

Digitization in Catalysis Research: Towards a Holistic Description of a Ni/Al₂O₃ Reference Catalyst for CO₂ Methanation

Sebastian Weber,^[a, b] Ronny T. Zimmermann,^[c] Jens Bremer,^[d] Ken L. Abel,^[e] David Poppitz,^[e] Nils Prinz,^[f] Jan Ilsemann,^[g] Sven Wendholt,^[h] Qingxin Yang,^[i] Reihaneh Pashminehazar,^[a] Federico Monaco,^[j] Peter Cloetens,^[j] Xiaohui Huang,^[k, l] Christian Kübel,^[k, l, m] Evgenii Kondratenko,^[i] Matthias Bauer,^[h] Marcus Bäumer,^[g] Mirijam Zobel,^[f] Roger Gläser,^[e] Kai Sundmacher,^[c, d] and Thomas L. Sheppard*^[a, b]

There is considerable motivation in the catalysis community and chemical industry to envision a future where rational catalyst design and targeted chemical process optimization become standard. Achieving this goal for heterogeneous catalysis requires a cultural shift centered around effective research data management. The core elements of modern catalysis research are synthesis, characterization, and testing, while all can be elevated by effective collection, correlation, interoperation, and exploitation of data between disciplines and stakeholders. Here, first steps are made towards a holistic picture of an industrial Ni/Al₂O₃

reference catalyst for CO₂ methanation. A range of conventional and advanced characterization tools are applied to probe metal particle size and pore characteristics of the support, selected as crucial parameters for catalyst performance. Challenges are shown with respect to current reporting of characterization data and metadata, which ultimately influences the development and reliability of digital twins in catalysis research. Furthermore, the cooperation and combined expertise of diverse research groups from different fields is recognized as essential to deliver meaningful progress towards the digital future of catalysis research.

[a] S. Weber, Dr. R. Pashminehazar, Dr. T. L. Sheppard
 Institute for Chemical Technology and Polymer Chemistry
 Karlsruhe Institute of Technology
 Engesserstraße 20
 76131 Karlsruhe (Germany)
 E-mail: thomas.sheppard@kit.edu

[b] S. Weber, Dr. T. L. Sheppard
 Institute of Catalysis Research and Technology
 Karlsruhe Institute of Technology
 Hermann-von-Helmholtz Platz 1
 76344 Eggenstein-Leopoldshafen (Germany)

[c] R. T. Zimmermann, Prof. K. Sundmacher
 Chair for Process Systems Engineering
 Institute of Process Engineering
 Otto-von-Guericke University Magdeburg
 Universitätsplatz 2
 39106 Magdeburg (Germany)

[d] Dr. J. Bremer, Prof. K. Sundmacher
 Department Process Systems Engineering
 Max Planck Institute for Dynamics of Complex Technical Systems
 Sandtorstraße 1
 39106 Magdeburg (Germany)

[e] K. L. Abel, Dr. D. Poppitz, Prof. R. Gläser
 Institute of Chemical Technology
 Universität Leipzig
 Linnéstraße 3
 04103 Leipzig (Germany)

[f] N. Prinz, Prof. M. Zobel
 Institute of Crystallography
 RWTH Aachen University
 Jägerstraße 17–19
 52066 Aachen (Germany)

[g] J. Ilsemann, Prof. Dr. M. Bäumer
 Institute of Applied and Physical Chemistry and MAPEX Center for Materials and Processes
 University of Bremen
 Leobener Straße 6
 28359 Bremen (Germany)

[h] S. Wendholt, Prof. M. Bauer
 Faculty of Science and Center for Sustainable Systems Design (CSSD)
 Paderborn University
 Warburger Straße 100
 33098 Paderborn (Germany)

[i] Q. Yang, Prof. E. Kondratenko
 Leibniz-Institut für Katalyse e.V.
 Albert-Einstein-Straße 29a
 18059 Rostock (Germany)

[j] Dr. F. Monaco, Dr. P. Cloetens
 ESRF – the European Synchrotron
 38043 Grenoble (France)

[k] X. Huang, Prof. C. Kübel
 Institute of Nanotechnology (INT)
 Karlsruhe Institute of Technology (KIT)
 Hermann-von-Helmholtz-Platz 1
 76344 Eggenstein-Leopoldshafen (Germany)

[l] X. Huang, Prof. C. Kübel
 Department of Materials and Earth Sciences
 Technische Universität Darmstadt
 Alarich-Weiss-Straße 2
 64287 Darmstadt (Germany)

[m] Prof. C. Kübel
 Karlsruhe Nano Micro Facility
 Karlsruhe Institute of Technology (KIT)
 Hermann-von-Helmholtz-Platz 1
 76344 Eggenstein-Leopoldshafen (Germany)

 Supporting information for this article is available on the WWW under <https://doi.org/10.1002/cctc.202101878>

 This publication is part of a joint Special Collection with ChemElectroChem on "Catalysts and Reactors under Dynamic Conditions for Energy Storage and Conversion (DynaKat)". Please check our homepage for more articles in the collection.

 © 2022 The Authors. ChemCatChem published by Wiley-VCH GmbH. This is an open access article under the terms of the Creative Commons Attribution Non-Commercial License, which permits use, distribution and reproduction in any medium, provided the original work is properly cited and is not used for commercial purposes.

Introduction

Efficient collection, correlation, interoperation, and exploitation of research data (herein defined as data management) is a growing concern in catalysis research.^[1,2] Considering only the branch of heterogeneous catalysis, data management bridges numerous disciplines including but not limited to: materials chemistry, inorganic and organic synthesis, crystallography, characterization based on spectroscopy, diffraction, or microscopy, computational chemistry, and real-world applications in chemical and process engineering. Growing awareness of the need for effective data management is evident within the academic sphere by the common inclusion of mandatory data-related content in funding proposals, affecting those on both the national (e.g., funded NFDI4Cat project within Germany^[2,3]) and international (e.g. European Commission funding^[4]) level. In modern heterogeneous catalysis research, catalyst characterization forms a central pillar and arguably possesses the strongest individual connection to the other two pillars, namely material synthesis, and performance testing or catalytic function. Characterization encompasses all manner of probes used to define the physical structure and chemical function of the catalyst. Understanding structure is naturally linked to the concept of rational catalyst design, while understanding chemical function leads to control and optimization of chemical processes for maximum benefit. All this can be considered as 'Holy Grail', or targets of extreme interest and value to the catalysis community and chemical industry. Consistent and effective management of characterization data is therefore a topic of urgent concern both now and in future research scenarios, regardless of the specific chemical process to which it is applied.

Aside from unavoidable errors such as differences in instrumentation or experience level of the user, various levels of complexity should ideally be considered during catalyst characterization. These include intrinsic heterogeneity of the catalyst sample, physical sensitivity (e.g., surface or bulk) or chemical sensitivity (e.g., crystalline or amorphous) of the measurement method, or in the case of spatially resolved analysis the effective resolution and/or dimensionality (e.g., 2D microscopy or 3D tomography) of the measurement. Additional complexity is present concerning *in situ* or *operando* methodology, whereby characterization and catalytic performance testing are coupled, and furthermore when considering transient or dynamic (rather than static) operating conditions, which may be relevant for real-world applications. For detailed and meaningful *in situ* and *operando* studies, a broad general characterization of the catalyst of interest is often a prerequisite. This might include general elemental analysis, textural/porosity studies, structural characterization and basic knowledge about the catalytic performance in the reaction of interest. The essential point is that no single characterization tool or strategy can adequately describe catalyst complexity in a sufficient manner to reach the ultimate aim of rational catalyst design and targeted chemical process optimization. Following this logic, a collaborative and inclusive effort of different research fields, connected by data

management, is of fundamental importance to ensure robust catalyst characterization. In the concept paper Catalysis 4.0, named after the imminent fourth industrial revolution (also known as Industry 4.0), Schlögl states that the research community is currently equipped with all necessary tools for accurate and complete description, prediction, and synthesis of optimized catalytic materials for targeted chemical processes.^[1] In other words, rational catalyst design and process optimization is already feasible, but further collaborative efforts are needed to address this challenge. In the context of characterization, initial efforts should focus on studying individual chosen reaction and catalyst pairings in as much detail as possible. However, this approach will only be meaningful when the diverse characterization data obtained is interrelated to be greater than the sum of its parts.

In the current work, we present early efforts towards thorough characterization of a target catalyst and reaction system, with the aim to demonstrate how collection and interpretation of characterization data relies on a diverse and interdisciplinary approach. The work is presented in the context of the collaborative research program 'DynaKat – Catalysts and Reactors under Dynamic Conditions for Energy Storage and Conversion'.^[5,6] Here we select methanation of CO₂ over an industrial standard Ni/Al₂O₃ catalyst (labelled SPP2080-IMRC) as a target material and process. SPP2080-IMRC in this respect stands for "Industrial Methanation Reference Catalyst" of the SPP2080 priority program^[6] of the German Research Foundation (DFG). In addition to being a useful starting point as a relatively facile gas-phase heterogeneously catalyzed reaction, CO₂ methanation is also an important topic in the context of chemical energy storage, future energy scenarios based on hydrogen economy and decentralized energy supply, and carbon management (where CO₂ is derived from waste emissions rather than direct capture). The chosen catalyst is intended as a reference point and benchmark between the diverse research consortia represented by the co-authors within the SPP2080 project. In terms of characterization, we selected two properties regarded as crucial for effective catalytic performance and which can be probed to a certain extent using multiple characterization methods. These are firstly the size distribution of active metal species, and secondly the pore system characteristics of the catalyst support. While the active sites are fundamentally responsible for catalytic reaction and turnover, the support properties govern the delivery of reactant molecules to, and product molecules from, these sites. The above parameters and their related characterization data are therefore ideal for an exploration into consistency of data and representativity of different characterization methods with respect to the catalytic active sites and support phase. This work highlights challenges associated with reporting information from catalyst characterization and performance testing. Tackling these are essential steps towards a "digital twin" of the catalyst. While no clear answer exists yet on how to overcome the challenges, the aim is to stimulate the whole catalysis community to find solutions together with other disciplines,

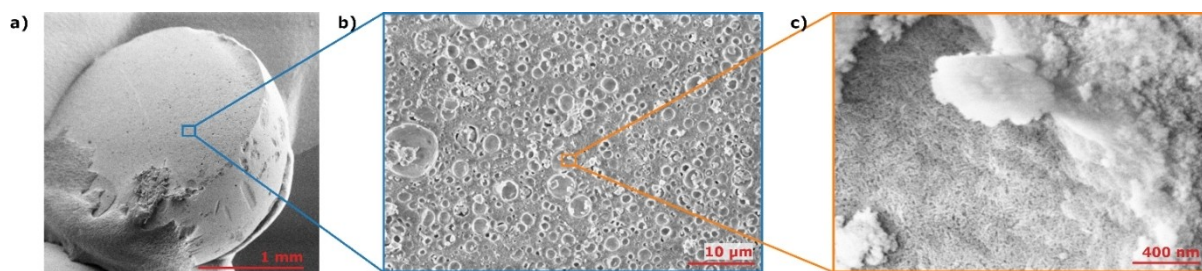


Figure 1. SEM images of a cut half sphere of the SPP2080-IMRC. (a) Overview of the cut half sphere, (b) magnified view indicating presence of spherical macropores, (c) further magnification indicates presence of mesopores in the material.

i.e., engineering, physics, material science, data science, mathematics, among others.

Results and Discussion

Porosity and Textural Properties

The SPP2080-IMRC catalyst particles are of approximately spherical shape as illustrated in the SEM image Figure 1a (cut half sphere) and the micro-X-ray computed tomogram (μ -XCT) of a single catalyst particle in Figure 3a. The particles have a spherical diameter of about 2.5 mm. The SEM images in Figure 1 indicate the presence of spherical macropores (Figure 1b) and mesopores (Figure 1c) in the material. One aim of this work is the detailed evaluation of the porosity within the SPP2080-IMRC, which is a basis for future simulation and modulation studies allowing for detailed description of the mass transport properties of the catalyst.

Conventional Porosity Characterization

The pore system of SPP2080-IMRC was first investigated by conventional porosity characterization methods operating on the bulk sample volume, i.e. N_2 sorption (Figure 2a,b) and Hg porosimetry (Figure 2c). The catalyst was investigated in powder form in addition to porosimetry of the whole pellet, to distinguish any influence of sample preparation on the macropores structures observed previously by SEM (Figure 1b). N_2

sorption isotherms of both pellet and powder (Figure 2a) can be described as type IV isotherms with a H1 hysteresis according to IUPAC classification,^[7] typical for mesoporous materials. A narrow pore width distribution is found by both methods, with maxima at 9.2 nm (both samples, N_2 sorption), 9.6 nm and 10.4 nm (pellet and powder sample, Hg porosimetry), respectively. The smaller pore width determined by N_2 sorption compared to Hg porosimetry can be explained by the systematic underestimation of the BJH method used in N_2 sorption for measuring mesopores < 20 nm.^[8] Notably, the N_2 sorption isotherms in Figure 2a do not reach a plateau at high p/p_0 values, indicating the presence of some additional pore volume. Apart from this, conventional porosimetry methods characterize the SPP2080-IMRC as essentially mesoporous, given the lack of distinct pore volume in the range of 50–10000 nm as probed by Hg porosimetry (Figure 2c). Complementary porosity values based on skeletal densities as measured by He pycnometry are given together with quantitative data from conventional porosity analysis in Table 1 and Table S1, ESI.

Despite the good agreement of N_2 sorption and Hg porosimetry data in terms of the pore width of SPP2080-IMRC, the specific pore volume determined by these methods exhibit large differences (Table S1, ESI). For both pellet and powder, the total pore volume from Hg porosimetry is more than $0.2 \text{ cm}^3 \text{ g}^{-1}$ larger when compared to the specific pore volume from N_2 sorption. These large differences indicate the presence of substantial network effects. Studying such network effects is in principle possible with Hg porosimetry by, for example, an analysis of the extrusion curve with varying dwell time at each data point.^[8] However, this is tedious and results may be

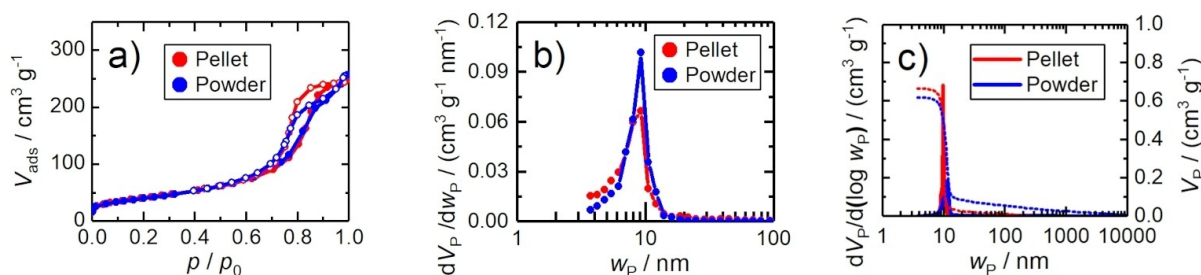


Figure 2. Conventional porosity data of SPP2080-IMRC pellet and powder samples; (a) N_2 sorption isotherms, (b) pore width distribution from N_2 sorption; (c) pore width distribution (solid lines) and cumulative specific pore volume (dashed lines) from Hg porosimetry.

Table 1. Results of the pore structure analysis of SPP2080-IMRC by conventional characterization (N_2 sorption, Hg porosimetry and He pycnometry) and tomography methods. For conventional characterization whole catalysts pellets and a crushed sieve fraction as powder (100–300 μm) were studied. The calculated parameters are specific surface area (A_{BET}), pore width by N_2 sorption (W_{p,N_2}), mesopore width ($W_{\text{p},\text{meso}}$), macropore width ($W_{\text{p},\text{macro}}$), mesoporosity (ϵ_{m}), macroporosity (ϵ_{M}) and total porosity (ϵ_{tot}).

	Pellet	Powder	Tomography
A_{BET} [m^2g^{-1}]	149	144	n.a. ^[a]
W_{p,N_2} [nm]	9.2	9.2	n.a. ^[a]
$W_{\text{p},\text{meso}}$ [nm]	9.6	10.4	14 ± 7 ^[b]
$W_{\text{p},\text{macro}}$ [μm]	n.a. ^[a]	n.a. ^[a]	1.43 ± 0.48 ^[c]
ϵ_{m} [%]	69.3	61.9	43.5 ^[d]
ϵ_{M} [%]	1.1	7.9	24.2 ^[c]
ϵ_{tot} [%]	70.4	69.8	65.7 ^[d]

[a] Not applicable; [b] from ET; [c] from HXCT; [d] from combined ET and HXCT results.

influenced by Hg remaining in the pores after each intrusion/extrusion analysis cycle. As the SEM images indicate the presence of macropores within the material, which were not found by conventional methods, the pore system of SPP2080-IMRC was additionally studied using 3D imaging techniques. In principle, analysis of the SEM images can also be used to estimate the macropore diameter, but this is limited to 2D information and depends on precise bisection of each macropore into a hemisphere, which is a disadvantage compared to the applied tomographic techniques.

Tomography-Based Porosity Characterization

To investigate all relevant length scales of the SPP2080-IMRC, a combination of different 3D imaging methods is necessary.^[9–12] For the pore system, length scales from nm to μm have to be covered, while the catalyst particle itself ranges to mm. The combination of different 3D imaging techniques was previously reported for several examples in order to study pore structures of catalysts and functional materials.^[9,13–19] Here, we selected laboratory X-ray microtomography (μ -XCT), synchrotron radiation-based holographic X-ray computed tomography (HXCT) and electron tomography (ET) as suitable techniques to cover relevant length scales from nm to mm as shown in Figure 3. The obtained quantitative results describing the pore structure based on the tomography methods are summarized in Table 1.

The μ -XCT of a whole SPP2080-IMRC particle shown in Figure 3a,b exhibits an isotropic voxel size of 2.67 μm . Therefore, the overall particle shape and large macropores can be studied by μ -XCT. Figure 3b shows the segmentation of the SPP2080-IMRC particle into porous solid (grey) and pores (orange) labels based on thresholding. The identified macropores are isolated and of spherical shape, as shown in Figure 3b. The porosity (ϵ) weighted equivalent spherical diameter (d_{eq}) distribution of the pores is plotted in Figure 3c. The general definitions of ϵ and d_{eq} for the tomograms are provided in eq. 4 and 5. The calculated porosity derived from μ -XCT is 0.7%. This indicates that only few macropores with

diameters above 3 μm are present in the sample, distributed rather homogeneously within the particle volume. However, as indicated by the SEM images (Figure 1) and the small porosity contribution in Figure 3c, smaller macropores are expected to be present. Therefore, the low resolution limit of μ -XCT is not enough to study the whole relevant macropore range.

To study macropores in the nm to the lower μm range, HXCT was performed on a crushed particle (diameter about 50 μm) of the SPP2080-IMRC after testing in CO_2 methanation reaction. The resulting HXCT volume data is shown in Figure 3d–f, with an isotropic voxel size of 25 nm. The estimated mean resolutions by fitting with a hyperbolic tangent function and by an edge-profile analysis (Figure S3, ESI) were ca. 94 nm and 54 nm, respectively. One can clearly identify the spherically shaped macropores of the catalyst, while different macropore sizes can be readily observed in Figure 3e,f. The ϵ weighted distribution of d_{eq} as plotted in Figure 3g reveals a mean d_{eq} of $1.43 \pm 0.48 \mu\text{m}$, while the overall porosity derived from the HXCT data is 24.2%, which is defined as the macroporosity (ϵ_{M}) obtained by 3D imaging (see Table 1). This clearly shows that the majority of macropores on the basis of volume are in the pore size range of about 0.5 to 2.5 μm (Figure 3g). The pores observed previously by μ -XCT are only a few larger macropores contributing relatively little to the particle porosity, which are also found as outliers within the HXCT porosity analysis (Figure 3g). It should be further noted that the macropores seem to be well separated in the HXCT data, similarly to the μ -XCT data.

To study the presence of mesopores (<50 nm), ET was carried out on two particles (ET1 and ET2, diameters about 400 nm) of the SPP2080-IMRC, which were selected and crushed after testing in CO_2 methanation reaction. The resulting ET volumes are shown in Figure 3h,i for ET1 and ET2, with isotropic voxel sizes of 0.29 nm and 0.58 nm, respectively. Contrary to the μ -XCT and HXCT results, a connected mesopore network was found in both ET volumes as shown in Figure 3h,i with the total pores label (orange). The mesopores identified by ET show no clear spherical shapes, which limits the representativeness of the d_{eq} analysis of separated pores applied previously for μ -XCT and HXCT data. Therefore, a pore network model of separated individually labelled pores (Figure S4, ESI) connected by pore throats was derived. The throat volume weighted distributions (d_{throat}) of the derived pore network models are plotted in Figure 3j for both ET. Mean d_{throat} values of 12 ± 7 nm and 15 ± 7 nm were found for the mesopore network in particles ET1 and ET2, respectively. These values can be compared with the mean d_{eq} values, which were larger with 16 ± 7 nm and 24 ± 8 nm for ET1 and ET2, respectively (Figure S4, Table S2, ESI). This confirms the overestimation of pore diameter by the d_{eq} spherical pore assumption for mesopores found by ET, validating use of the pore throat values as an alternative. The ϵ values of ET1 and ET2 are 56.4% and 58.4%, respectively. The average of the mean d_{throat} of the two ET volumes is taken as the mesopore width ($W_{\text{p},\text{meso}}$), while the mesoporosity (ϵ_{m}) of 43.5% was calculated using the average of the ϵ for ET1 and ET2, and considering the nanoporous solid of the HXCT volume to have that porosity.

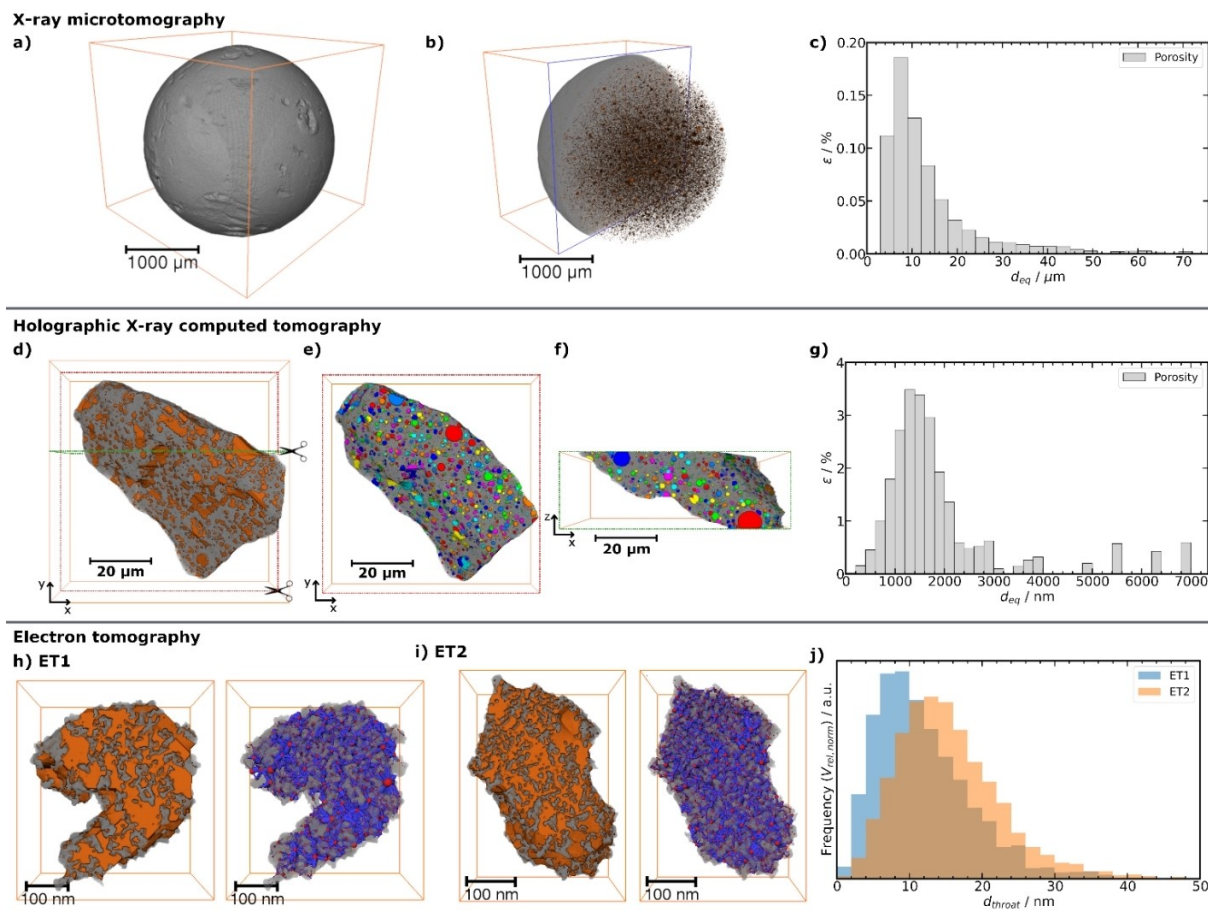


Figure 3. Characterization of the pore structure of the SPP2080-IMRC catalyst by X-ray microtomography (μ -XCT, a–c), holographic X-ray computed tomography (HXCT, d–g) and electron tomography (ET, h–j). (a) volume rendering of the SPP2080-IMRC particle studied by μ -XCT, (b) illustration of the porous solid (grey) and pores (orange) labels after segmentation, with a cut of the porous solid label to highlight the pores, (c) porosity (ϵ) weighted distribution of the equivalent spherical pore diameter (d_{eq}) of the macropores identified by μ -XCT. (d) volume rendering of segmented HXCT data with nanoporous solid (grey) and pores (orange) labels, (e, f) cuts through the volume with individually labelled pores (8 bit color code) and nanoporous solid (grey) showing isolated spherical macropores, (g) porosity (ϵ) weighted distribution of d_{eq} of the pores identified by HXCT. (h, i) Volume rendering of ET data from two different sample particles (ET1, ET2), each showing the whole particle with solid (grey) and pores (orange) labels and derived pore network models with solid (grey), individual pores (red) and connecting pore throats (blue), (j) throat volume weighted distribution of the pore throat diameter (d_{throat}) of the ETs.

Comparison of Conventional and Tomography-Based Porosity Characterization

The present case clearly illustrates the importance and power of applying advanced imaging techniques in addition to conventional methods when attempting to characterize the pore structure of catalysts. Conventional methods, i.e., N_2 sorption and Hg porosimetry failed to reveal significant presence of macropores within the SPP2080-IMRC, neither in pellet nor powder form. While the obtained total porosities (ϵ_{tot} , Table 1) are well in agreement for conventional and imaging-based characterization, the distribution of pore sizes constituting the total porosity were very different. Tomography studies showed significant presence of macropores accounting to a macroporosity of 24.2%, which was not found by N_2 sorption and Hg porosimetry. This might be explained by the isolated nature of the spherical macropores identified by imaging studies, which most presumably are connected to each other by a mesopore network as observed by ET. This would additionally explain the

agreement of the ϵ_{tot} between tomography and conventional methods, as especially Hg porosimetry probes the pore opening rather than the pore body.^[8] The d_{throat} analysis of the ET data is close to the values found by conventional characterization methods and thus $w_{p,meso}$ (Table 1) matches quite well between the methods. However, the d_{eq} analysis of the ET results in significantly larger pore sizes, which might be explained by incorrect assumption of spherical pore shapes, or sensitivity to the pore body rather than the pore throat. This is contrary to mathematical assumptions of the conventional methods, while such differences between tomography and conventional characterization have been reported previously.^[15]

In general, differences of the results obtained by tomography and conventional characterization of catalyst pore structures are commonly known,^[13,15,20–22] while the present example in this study is an extreme case. However, if the SPP2080-IMRC should serve as a reference material and to create a “digital twin” of the material, a detailed and correct knowledge of the pore structure is inevitably needed. An

incorrect pore model would result in inaccurate descriptions of heat and mass transport in the “digital twin”, which would further complicate reaction kinetics studies based on comparing modelling and empirical data. As shown here, roughly 33% of the total porosity would be incorrectly defined by relying only on conventional methods, i.e., N_2 sorption or Hg porosimetry. In this respect, it can be concluded that relying only on conventional analysis and reporting or using only mean values of parameters such as mean pore diameter will not provide sufficient detail to allow creation of an accurate digital model for a given material in the future. However, the same is arguably also true for advanced pore characterization techniques when applied individually to complex hierarchically porous samples. For example, ET completely fails in this example to characterize macropore or large mesopore structures, since these are on the same length scale as the entire sample body which can feasibly be measured when using electrons as the probe. On the other hand, even hard X-ray nanotomography methods such as HXCT applied at the most modern synchrotron light sources available cannot currently provide sufficient resolution to analyze small mesopores or micropores. The logical conclusion is that the complementary characteristics and applicable length scales of different tomographic methods should optimally be combined to produce an accurate description of porosity in complex samples. As advanced imaging techniques are only local techniques compared to the conventional ones, a careful sample selection is required ensuring highest possible representativity of the selected sample compared to average information from conventional methods. The generation of a “digital twin” based on ET analysis using also information like connectivity or constrictivity was recently reported for the mesopore network of porous silica, although only as a model system.^[23] Based on the tomographic characterization future development of sophisticated pore network models, e.g., creation of imaging based mathematical models,^[23] resistor networks,^[24] or others are possible but out of scope of this work. In the current work, the reconstructed segmented tomograms are available online and are open access, which helps to facilitate the development of advanced pore network models in the future. The pore network models that can be obtained from imaging studies can be applied for a detailed description of mass transport phenomena in the catalyst, allowing different levels of complexity.^[22]

Elemental and Structural Analysis

Elemental Analysis

Elemental analysis of the catalysts was carried out by ICP-OES. The Ni content of the catalyst is 8.6 wt.%. Furthermore, Ca, Co, Cr, Cu, Fe, Mg, Na, and Zn were determined. While those elements were below the detection limit, only Fe was present in traces of 0.01 wt.%.

Transmission Electron Microscopy (TEM) Studies

The Ni particle size of the SPP2080-IMRC was investigated by TEM as shown in Figure 4. For TEM studies, a spent catalyst sample after testing in CO_2 methanation reaction conditions up to 673 K was studied. In Figure 4a,b the exemplary bright field (BF) and HAADF-STEM images clearly show the presence of small Ni nanoparticles with diameters below 2 nm. 875 Ni particles were analyzed using eight different HAADF-STEM images resulting in the Ni particle size distribution shown in Figure 4c and a calculated mean Ni particle size of $0.8 \text{ nm} \pm 0.4 \text{ nm}$ in the SPP2080-IMRC after catalytic testing.

Powder X-ray Diffraction (PXRD) and Pair Distribution Function (PDF) Analysis

The PXRD shows broad Bragg reflections that fit the theoretical calculated powder pattern of $\gamma\text{-Al}_2\text{O}_3$ (Figure 5a). As shown above ICP-OES detected 8.6 wt.% Ni, which corresponds to 10.9 wt.% NiO or 14.4 mol% NiO. This phase is hardly visible in the PXRD. After reduction in 25 vol.% H_2 for 1 h at 773 K, a Ni_{fcc} phase evolves. Again, the phase shows low signal and broad Bragg peaks, which are indicative of a very small Ni particle size. This makes total scattering analysis necessary for further investigation of the Ni species, since the relevant Bragg peaks overlap strongly with those of the porous $\gamma\text{-Al}_2\text{O}_3$ support.

PDF analysis is a powerful method to characterize nanoscale materials. The PDF is obtained by Fourier transformation of the total scattering signal and represents the histogram of all interatomic distances in the sample. Hence, it is perfectly suited

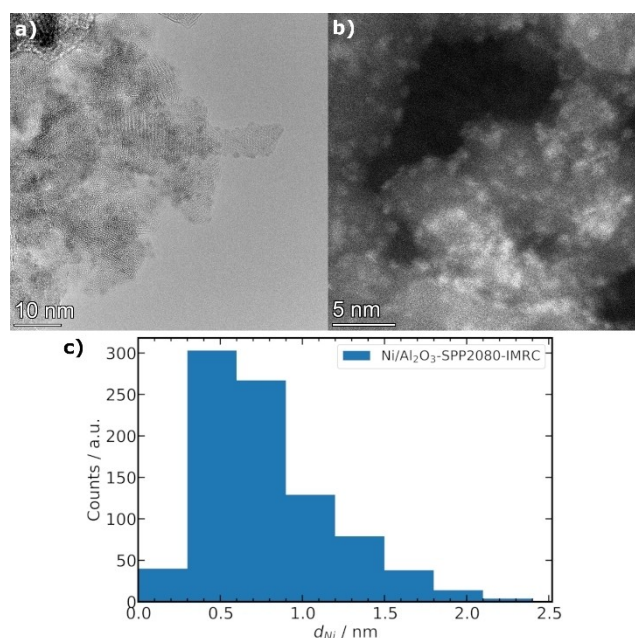


Figure 4. (a) Bright field (BF)-TEM and (b) HAADF-STEM images of the SPP2080-IMRC after testing in CO_2 methanation reaction showing small Ni nanoparticles. (c) Ni particle size distribution (total of 875 Ni particles) for the analysis of eight different HAADF-STEM images.

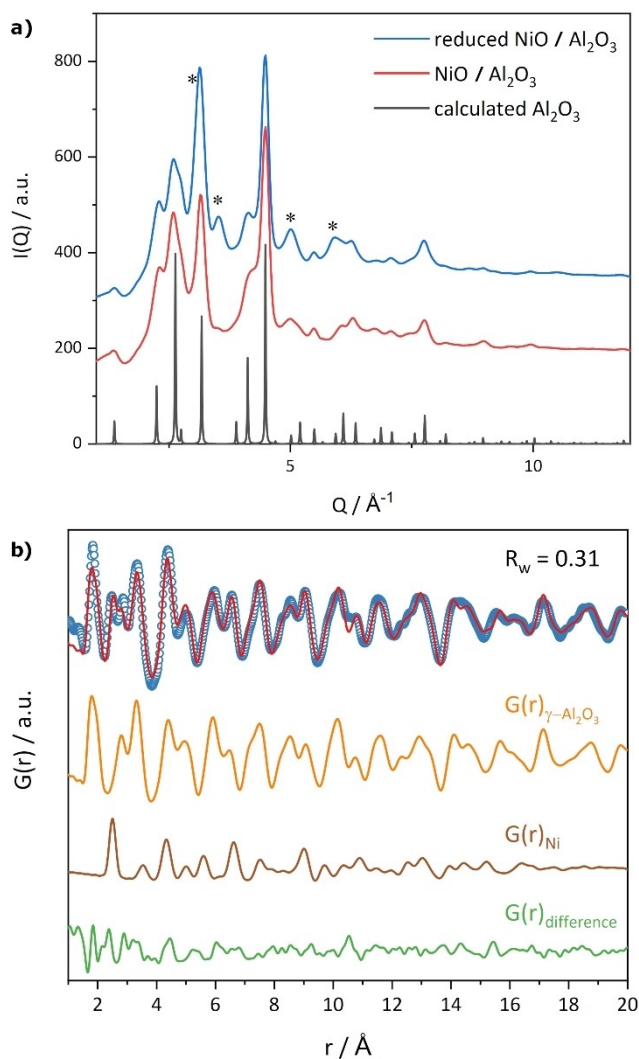


Figure 5. (a) PXRD with broad peaks for Al_2O_3 and calculated powder pattern for comparison. The NiO and Ni phase consist of broad humps. The visible Bragg reflections of the Ni phase in the reduced catalyst are denoted by stars. (b) Two phase PDF refinement of reduced catalyst using Ni_{fcc} (brown) and $\gamma\text{-Al}_2\text{O}_3$ (orange) as a starting structure. The difference (green) between experimental data (blue circles) and refined data (red curve) lead to a R_w of 0.31.

to characterize the catalyst material, which contains a defect-rich $\gamma\text{-Al}_2\text{O}_3$ support and very small Ni nanoparticles. For elucidating the contributions of the active phase, a two-phase refinement is used for the inactive pre-catalyst ($\text{NiO}/\gamma\text{-Al}_2\text{O}_3$) (see Figure S5, ESI) and the active catalyst after reduction with H_2 ($\text{Ni}/\gamma\text{-Al}_2\text{O}_3$, Figure 5b). For the Al_2O_3 phase, a cubic (inverse spinel) $\text{Fd}\bar{3}\text{m}$ crystal structure is employed as a starting structure with Al^{3+} cations on tetrahedral and octahedral spinel positions, as well as additional Al^{3+} cations on non-spinel positions.^[25] A $\text{Fm}\bar{3}\text{m}$ space group was used in case of the NiO and Ni phases. For all phases, the refined parameters comprise the lattice and isotropic thermal parameters, as well as a dampening function, which accounts for spherical particles of finite crystallite size. The domain size is visible in the decaying $G(r)$ signal for increasing distances. For both refinements, a

goodness of fit $R_w=0.31$ was achieved, which is an adequate value, given the defect-rich support material. The lattice parameter and thermal parameters of Al_2O_3 are larger in the active $\text{Ni}/\text{Al}_2\text{O}_3$ because it was measured at 673 K instead of 298 K. The molar content of the NiO and Ni phase is refined to 14%, and 19%, respectively, matching well the ICP-OES results. As a volume method, the PDF is well-suited to characterize small average particle sizes. For NiO the particle size is refined to 1.9 nm. By calculating the Ni-density in NiO and Ni, a particle size of 1.1 nm is expected after reduction, similarly to the TEM results on an activated catalyst sample. Instead, the particle size increases after reduction to 3.2 nm. This highlights that some sintering might have occurred in the reduction step. The refined particle size of Ni in the active catalyst is larger than observed by TEM (ca. 0.8 nm). The size difference of the Ni species in the activated SPP2080-IMRC between TEM and PDF data of ca. 2 nm might be explained by different reasons. First, the activated samples were obtained by different treatments, i.e., for PDF analysis *in situ* activation in a capillary reactor with 1 mm diameter equipped with a hot-air blower was used, while for TEM, the sample was treated in a laboratory continuous flow reactor with an active temperature control (setup description in Ref. [26]). Although the hot-air blower was calibrated using a thermocouple, the absolute temperature cannot be controlled precisely as in the laboratory reactor and inhomogeneous heating by the hot-air blower (bottom is hotter than top of the capillary) cannot be avoided. This problem is known in the community and such gradients might easily span more than 40 K from the bottom to top of the reactor.^[27] Both effects can lead to unwanted higher temperatures than the applied 773 K during the reduction step and consequently to more sintering in the reduction step. This highlights that precise reporting of specific reactor setups and typical operating conditions within or between those setups should be considered as essential metadata in the catalysis community, which is often not adequately performed.

The parameters of the Al_2O_3 phase are refined to very similar values for the two samples, underlining the robustness of the refinement strategy. The Al^{3+} cations occupy 27% and 30% non-spinel positions in the $\text{NiO}/\text{Al}_2\text{O}_3$ and the reduced $\text{Ni}/\text{Al}_2\text{O}_3$ sample, respectively. Notably, the difference curves of the two refinements are very similar, indicating that the residual structural signal in the difference curves stem from the Al_2O_3 phase. To explore this further, we aimed to eliminate the Al_2O_3 contribution by calculating a difference-PDF (d-PDF), for which we subtract the scattering signal of the $\text{NiO}/\text{Al}_2\text{O}_3$ sample from the reduced $\text{Ni}/\text{Al}_2\text{O}_3$ sample during PDF calculation. Hence, the resulting d-PDF contains positive contributions from Ni and negative contributions of NiO, as the NiO is entirely reduced to Ni in the reduction step and thus disappears. The d-PDF refinement with Ni as positive and NiO as negative phase leads to a better goodness of fit of $R_w=0.24$ (see Figure S6, ESI), confirming the assumption that short-range disorder of the Al_2O_3 is present, which is not adequately described by the model used for the Al_2O_3 .^[25] The values for the refined parameters of the Ni phase in the d-PDF fit and in the two-phase fits are in good agreement (see Table S3, ESI). The values

for the average displacement parameters B_{iso} for the NiO are slightly higher with 1.01 \AA^2 vs 0.42 \AA^2 and 2.09 \AA^2 vs 1.44 \AA^2 for $B_{\text{iso}}(\text{Ni})$ and $B_{\text{iso}}(\text{O})$, compared to the 2-phase fit. The particle size is with 2.4 nm slightly higher than 1.9 nm in the 2-phase fit. The lattice parameter a was refined to 4.171 \AA , which is around 0.013 \AA lower than in the 2-phase fit, but is in better agreement with literature values for the lattice parameter of cubic NiO.^[28]

X-ray Absorption Spectroscopy (XAS) Studies

XAS is a powerful tool to characterize amorphous materials, due to its short-range sensitivity.^[29,30] The XANES (X-ray absorption near-edge structure) region of a XAS spectrum gives information about the oxidation state of the absorbing atom and the local structure in a fingerprinting manner. In Figure 6a, the XANES spectra obtained of the non-activated and activated

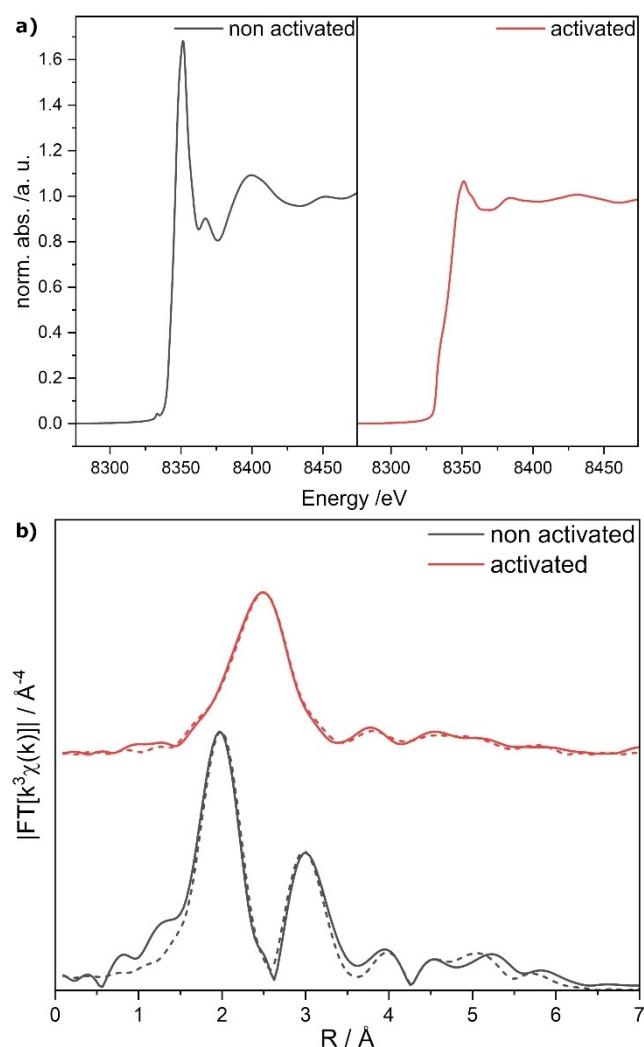


Figure 6. (a) Ni K-edge XANES spectra of the SPP2080-IMRC. The non-activated catalyst was measured *ex situ* in transmission mode, and the activated catalyst measured *in situ* in fluorescence mode. (b) Fourier-transformed experimental $k^3\chi(k)$ EXAFS functions of the SPP2080-IMRC. Solid lines show experimental spectra and dotted lines show the theoretical fits from EXAFS analysis.

species of the catalyst are shown. Hereby it can be seen that the edge position shifts from 8345 eV which is typical for Ni(II)-species, to 8333 eV which indicates Ni(0)-species. The observed shape of the activated species is quite comparable to those seen for decomposed MOF pre-catalysts in previous work. For these pre-catalysts, a mixture of Ni(0) and Ni(II) species are present on carbon support.^[31]

Further EXAFS analysis was performed to get information about structural parameters (see Table S4, ESI). Figure 6b shows the Fourier-transformed EXAFS spectra of the investigated samples. The inactive form (NiO/Al₂O₃) of the catalyst was measured *ex situ* as a pellet in transmission mode. 6 Ni–O pairs at 2.05 \AA fit to literature values of NiO^[32] and NiO/Al₂O₃ in literature (2.06 \AA),^[33] especially if these results are compared with smaller NiO particles, since the Ni–O distance decreases with smaller particle size.^[34] Also, the Ni–Ni distance of 2.96 \AA in the 2nd shell fits the literature distance of 3.0 \AA .^[33] However, the Ni–Al pair around 4.0 \AA shows a different distance than the literature (4.13 \AA).^[35] Noticeable is the intense peak for Ni–O distance around 2 \AA and less intense peak around 3 \AA is reversed for NiO without support, meaning that Ni–Ni peak is more intense than the Ni–O signal.^[32,34] Such an effect has been observed previously by Shido et al. for Ni/Al₂O₃ catalysts.^[35]

The activated catalyst was measured after reduction with H₂ *in situ* in a capillary setup in fluorescence mode. Even though no further changes in XANES were observed at this point, there is still some Ni–O at 1.97 \AA visible which is necessary for a good fit. Additionally, the Ni–Ni distance from NiO at 2.96 \AA is still needed. For Ni(0) species, a Ni–Ni pair at 2.45 \AA can be found, which fits the Ni_{fcc} distance. The 1.5 Ni–O pairs are referring to $\frac{1}{4}$ of a full NiO 1st shell (6 pairs), 5.7 Ni–Ni pairs, on the other hand, are roughly half of a full Ni_{fcc} first shell of 12 atoms. This means the results are consistent with a mixture of both species as also observed in XANES data. The Ni–Ni distance of 3.44 \AA is smaller than in bulk Ni_{fcc}, which could be a particle size effect indicating the presence of small nanoparticles, in line with the TEM and PDF results. This is supported by the fits of higher distances in the activated species, since the coordination numbers are lower than in bulk Ni. These fits result in Ni with higher vacancies, due to small particles.^[32,34] Overall typical distances of Ni_{fcc} and NiO^[32,34] as well as Ni/Al₂O₃^[35] were found.

Temperature-Programmed and Surface Analysis

Temperature-Programmed Reduction (TPR)

The H₂-TPR profiles for SPP2080-IMRC powder and spheres (samples coincide with those from conventional porosity analysis) are compared with a physical mixture (PM) of NiO and Al₂O₃. To ensure good comparability, all samples contain similar Ni loadings, which are used to normalize the TCD signal in Figure 7. NiO typically reduces to Ni⁰ between 473 and 573 K , depending on particle size, support material and confinement within pores.^[36,37] Correspondingly, the physical mixture of NiO powder and Ni-free Al₂O₃ shows a reduction peak with a maximum at 545 K . The SPP2080-IMRC samples also exhibit

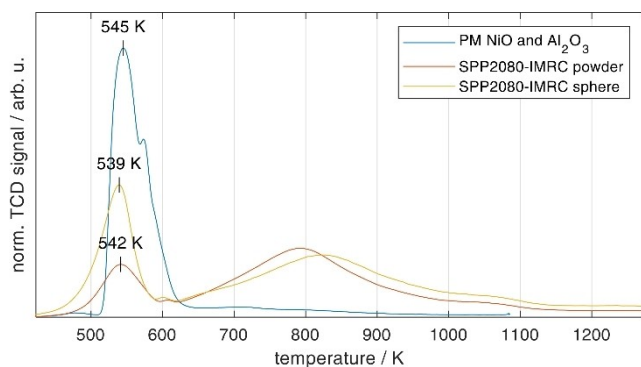


Figure 7. TPR profiles for the SPP2080-IMRC (56 mg, $\omega_{\text{Ni}} = 8.6$ wt.%) powder, sphere, as well as a physical mixture (PM) of NiO and Al₂O₃ (54 mg, $\omega_{\text{Ni}} = 8.2$ wt.%), profiles show the normalized intensity of the thermal conductivity detector (TCD) by the corresponding Ni mass, $dT/dt = 10 \text{ K min}^{-1}$, $F_{\text{H}_2/\text{Ar}} = 30 \text{ NmL min}^{-1}$, 10 vol.% H₂ in Ar.

pronounced peaks close to the maximum of the physical mixture, indicating significant amounts of bulk NiO. Earlier reduction signals might be an indication for the presence of Ni₂O₃.^[38] In contrast to the physical mixture, the SPP2080-IMRC additionally displays a broad TCD signal between 623 and 1173 K. The peak slightly above 773 K typically corresponds to Ni²⁺ incorporated into octahedral voids in the alumina lattice^[39] or into the NiAl₂O₄ framework,^[38] while a distinction between both is difficult due to similar crystallographic structures. In both configurations, the reduction of Ni²⁺ to Ni⁰ is inhibited due to its strong binding within the crystal. The partial incorporation is also supported by Ni–Al interactions found by XAS and the absence of clear NiO reflections in the PXRD. Therefore, it can be assumed that Ni is present as small NiO particles as well as partly incorporated into the support structure.

H₂ Chemisorption and CO₂ Temperature-Programmed Desorption with Diffuse Reflectance Infrared Fourier Transformed Spectroscopy (DRIFTS)

For an accurate and holistic description of the employed catalyst, information regarding the number of potential active sites for H₂ and CO₂ adsorption and their nature is required. Regarding the former, pulsed chemisorption experiments were carried out and the results are compiled in Table 2. Directly after saturating the surface with CO₂ by pulsed chemisorption, a temperature-programmed desorption (TPD) experiment was used to determine the adsorption strength of the adsorbed species, while DRIFTS were performed in parallel to unravel the

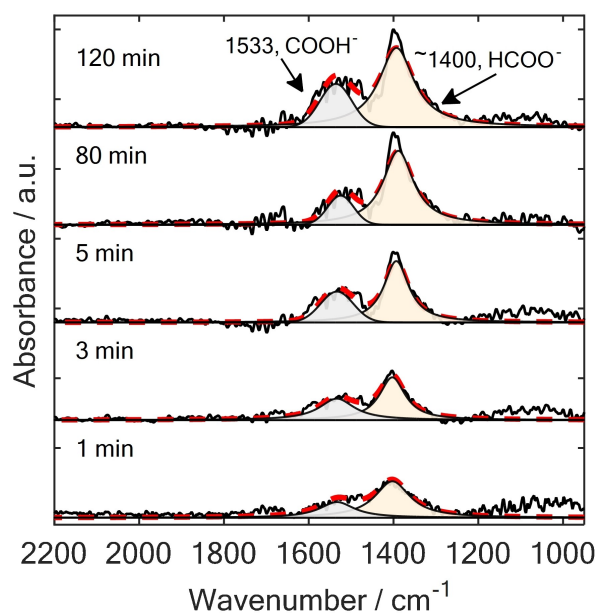


Figure 8. DRIFT spectra after exposing the catalyst to 2 vol.% CO₂ in He at 303 K. Black solid line: measured spectra, blue shaded area: fitted peak for carboxylates (COOH⁻), red-shaded area: fitted peak for formates (HCOO⁻), red dashed line: sum spectra.

CO₂ adsorption configuration allowing to characterize the nature of the active sites further. For an adsorbed species to be relevant in the catalytic turnover, its binding strength can neither be too weak, i.e. it desorbs at temperatures below the catalytic onset temperature, nor too strong as an excessive adsorption strength would lead to catalyst poisoning. In fact, previous research has proven the beneficial effect of sites with “intermediate” CO₂ adsorption strength from which CO₂ would desorb at temperatures between 473 and 673 K corresponding to expected reaction temperatures for the CO₂ methanation.^[40,41] The CO₂ desorption trace (Figure S8, ESI) shows two distinct desorption peaks – a small, yet sharp peak at around 373 K indicative for sites where CO₂ binds only weakly and a second significantly larger feature centered around 598 K corresponding to adsorption sites, which exhibits the desired intermediate basicity. In line with the previous results, the DRIFTS analysis (Figure 8) of the CO₂ adsorption configuration reveals the formation of two different species – formate (HCOO⁻) and carboxylate (COOH⁻) as indicated by the absorption bands at 1400 and 1533 cm⁻¹, respectively.^[42,43] The absence of any features related with carbonate species even after a prolonged exposition time of 120 min suggests that either species is formed via a mechanism involving CO₂ adsorption on Al^{VI}_{CUS} sites at the metal-support perimeter

Table 2. Summary of the CO₂ and H₂ chemisorption experiments performed at 303 and 323 K, respectively. The metallic surface area and metal dispersion are calculated based on the H₂ chemisorption measurements according to eq. 1 and 2. The experimental error was estimated based on the standard deviation determined in three consecutive H₂ chemisorption experiments.

	CO ₂ uptake [$\mu\text{mol g}^{-1}$]	H ₂ uptake [$\mu\text{mol g}^{-1}$]	Metallic surface area [$\text{m}^2 \text{g}^{-1}$]	Dispersion [%]
Ni–Al ₂ O ₃	62	77 ± 5	6.0 ± 0.4	10.1 ± 0.6

followed by a rapid hydrogenation with residual H atoms spilling over to the perimeter, rather than a mechanism involving CO₂ adsorption as carbonate species.^[44,45]

Catalytic Activity Studies

Two different catalytic testing approaches are considered. First, long-term activity tests were conducted with crushed SPP2080-IMRC powder at low temperatures, low flow rates and high pressures. On the other hand, short-term activity tests with SPP2080-IMRC in its original shape and the crushed powder are conducted at higher temperature and flow rates, but at lower pressures. Additionally, the results of the latter are compared to kinetic models from literature. Due to the different test conditions, evidence about the catalyst behavior over a wide operating range is possible.

Catalytic Testing Results from the Parallel Tubular Fixed-bed Reactor System

The catalyst was tested at different reaction temperatures (473–573 K) as shown in Figure 9a. Both CO₂ conversion and selectivity to CH₄ were almost unchanged with time-on-stream at each reaction temperature. The contact time was varied by using different catalyst amounts to achieve different degrees of CO₂ conversion (Figure 9b, Figure S9a, ESI). Moreover, CO₂ conversion increased along with the reaction temperature until 523 K and tended towards the thermodynamic equilibrium at higher temperatures (Figure S9a, ESI). CH₄ was found to be the main product with the selectivity above 98.9%, regardless of the reaction temperature and contact time (Figure 9a, Figure S9b, ESI). No CO was observed, whereas minor amounts of

ethane and propane were formed with the total selectivity below 1.1 % (Figure S9b, ESI).

Catalytic Testing Results in a Single Tubular Fixed-bed Reactor

As shown in Figure 10, the SPP2080-IMRC behaves very differently in its original spherical shape compared to the powder. In both cases, measurable CO₂ conversions (Figure 10a) are present at temperatures of 523 K, which increase with temperature. In the powder case, the conversion rises much quicker and approaches the thermodynamic equilibrium as the temperature rises to 773 K. At 773 K, the catalyst powder converts about twice as much CO₂ as the spheres, thus indicating a strong influence of mass transport limitations in the spheres. The same can be observed for the formation rate of the products CO and CH₄, which is expressed by the CH₄ selectivity (Figure 10b). The catalyst spheres show the highest CH₄ selectivity at low temperatures, which significantly decreases with increasing temperature. The catalyst powder behaves similarly at temperatures up to 623 K, where a local minimum of CH₄ selectivity is present. At higher temperatures, the selectivity increases again until reaching a local maximum before decreasing again. Accordingly, the powder shows a higher CH₄ selectivity for temperatures above 647 K. Based on the observed mass transport limitations, further detailed macrokinetic studies are required to understand the reason for them in connection to the catalyst pore structure.

The methanation kinetic models of Burger et al.^[46] (coprecipitated catalyst, 44 wt.% NiAlO_x) and Lalinde et al.^[47] (OMA-30Ni-500, ~30 wt.% NiO on Al₂O₃) were extrapolated to the conditions of this study. Assuming that the powder measurements represent the intrinsic kinetics, the SPP2080-IMRC is far more active than the catalyst used by Lalinde et al.,^[47] but less selective up to a temperature of about 673 K. Compared to the

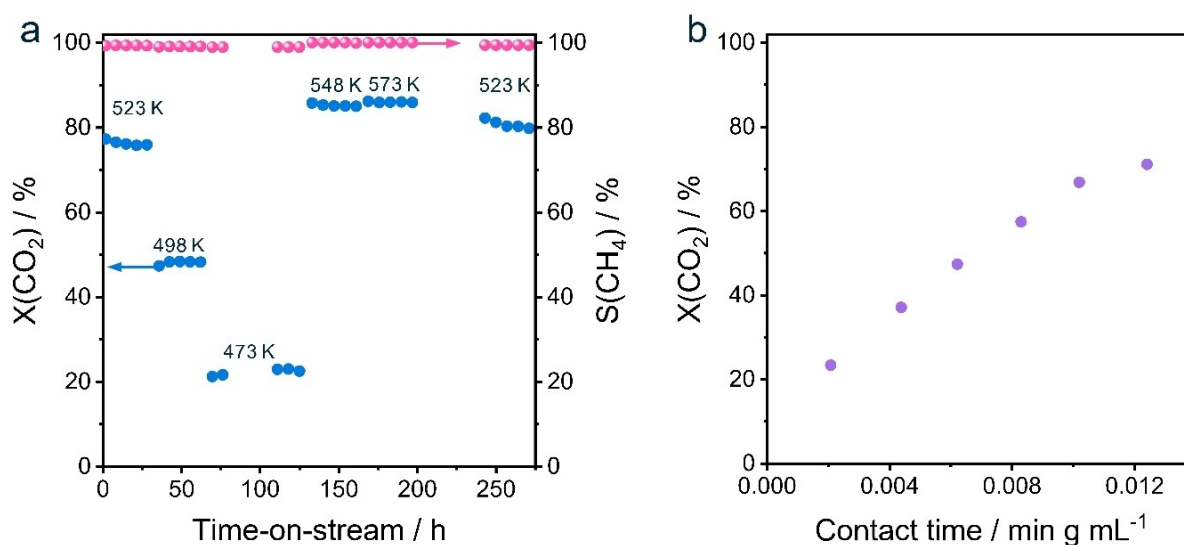


Figure 9. (a) Conversion of CO₂ (blue) and CH₄ selectivity (red) as a function of time on stream at different reaction temperatures. Reaction conditions: $m_{\text{cat}} = 0.075$ g, 473–573 K, 10 bar, H₂/CO₂/N₂ = 0.8/0.2/9, flow rate = 12 mL min⁻¹. (b) The conversion of CO₂ as a function of contact time at 498 K.

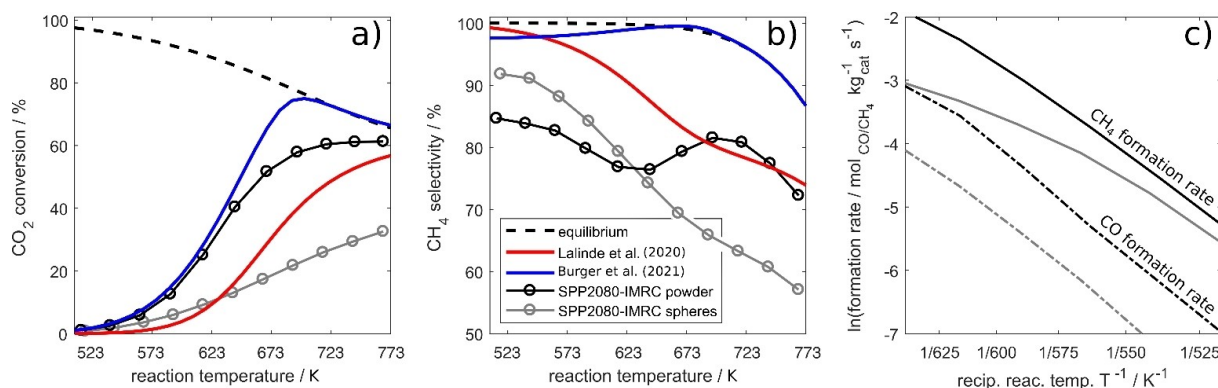


Figure 10. CO₂ conversion (a), CH₄ selectivity (b) as well CH₄ and CO formation rates (c) for SPP2080-IMRC spheres and powder. Reaction conditions: $m_{\text{cat}} = 0.030$ g, 523–773 K, 1.2 bar, H₂/CO₂/He = 0.1/0.4/0.5, flow rate = 200 mL min⁻¹.

catalyst used by Burger et al.,^[46] the SPP2080-IMRC is also far less selective and less active. However, it should be noted that the SPP2080-IMRC also exhibits a smaller Ni mass fraction of 8.6 wt.% (Lalinde et al. 23.6 wt.%,^[47] Burger et al. 44 wt.%^[46]).

For a deeper understanding of how the catalyst particle size influences the product formation rates, Arrhenius plots in a temperature range from 523 to 623 K are given in Figure 10c. This temperature range is assumed to be sufficiently far from the thermodynamic equilibrium, such that it does not influence the reaction rates. In the Arrhenius plot, the CO formation rate (dash-dotted lines) of both powder and spheres show approximately the same slope, indicating no significant influence of the particle size on the temperature dependence of this component formation rate. Only the CH₄ formation rate of the spheres (solid gray line) significantly deviates from a straight line and, thus, indicates a strong influence of the particle size and the corresponding mass transport limitation. The reason for the different behavior of the formation rates is the result of the complex interplay of reaction and diffusion kinetics within the catalyst particles. However, further kinetic studies are necessary to explain this result in detail.

In summary, by using two different catalytic setups, the SPP2080-IMRC was tested at various conditions. The catalyst was found to be stable over a time period of at least 11 days. The activity and selectivity of the crushed catalyst spheres is comparable to those found in literature. For all experimental conditions, CH₄ was the main product, but CO started forming at elevated temperatures in significant amounts. Ethane and propane could also be detected in minor amounts. Furthermore, significant differences in the catalytic performance between the spheres and crushed powder are present, which were traced back to the influence of mass transport limitations.

Summarized Discussion of the Results in the Frame 'Digitization in Catalysis Research'

Progressing from individual investigation of catalysts or reactions, towards concerted efforts in terms of rational catalyst design and targeted process optimization, is a monumental

challenge facing the catalysis community and chemical industry. The current work demonstrates the scale of cooperation needed to address these challenges for a single specific case study. In heterogeneous catalysis research, there are several layers of information which are important to consider: (i) synthesis parameters and post-synthetic treatment/modification, (ii) characterization data along with instrumental and measurement related metadata, (iii) catalytic performance data (activity, selectivity, yield, turnover) along with instrumental and measurement related metadata. As the catalyst used throughout this work comes from a single batch of an industrial reference sample, synthesis parameters can be regarded as a constant, leaving the main focus on catalyst characterization. However, catalytic studies involving synthesis should carefully consider point (i) as one of the three layers of information.

The purpose of characterization and correlating catalytic performance with materials properties of the catalyst, is to promote an in-depth understanding of catalytic function and operation. According to the blueprint of Catalysis 4.0,^[1] rational catalyst design, the creation of digital twins for target catalysts and processes, and the proper integration of data and metadata in the context of catalysis research are the end goals. An essential part of the 'intermediate solution' is to examine individual systems thoroughly, in as much detail as possible, and to combine or interpret the knowledge as a whole. An important realization demonstrated here is that collaborative efforts with diverse expertise are key aspects, while accurate reporting of all data and metadata (e.g., instruments, operating parameters, reaction steps, etc.) is essential.

The present work identifies the accuracy of characterization data as a central challenge, since typically only the precision can be derived from common statistical analysis. The appropriateness or validity of selected characterization techniques for answering specific questions (e.g., porosimetry and tomography for pore characterization, or XAS, XRD, PDF and TEM for nanoparticle size analysis) needs to be carefully considered, especially when individual techniques are used in isolation. Furthermore, the common interpretation of single (often bulk) values to describe complex material properties is certain to be inadequate in the future. A strong example of this is with

porosity characterization, in which conventional porosimetry does provide an accurate measure of total porosity, but completely fails to distinguish different contributions of each pore length scale on the total value, for which tomography analysis is required. Therefore, the currently accepted norm of comparing single (bulk) parameters obtained from individual characterization techniques as the basis for catalyst design, benchmarking of catalytic performance, or selection of lead candidates for further investigation may be inherently flawed. Additionally, ways have to be found to evaluate the quality of collected characterization data, which is difficult. For selected examples, like databases of XRD based crystal structures, this is already incorporated to a certain extent. However, it is not possible to use this simply as a blueprint for other techniques, so proposing and establishing quality checks is an open challenge for the community.

A first attempt towards improving catalyst characterization could be to investigate and apply distributions of values for specific catalyst features (e.g., particle size, dispersion, pore diameter/volume) instead of single mean values with statistical errors. More complex ways of comparing data and critically evaluating the applicability of techniques for different material types, will have to be developed in future. As shown with different mean Ni particle sizes found by TEM, PDF and H₂ chemisorption analysis, it is clear that sample history, measurement conditions, and most probably instrumental differences can have a strong influence on the result, even when measuring the same catalyst batch. The current work cannot simply state which of the obtained values is the correct one, but rather shows that single values and 'preferred' characterization methods may not provide all necessary information. Further usage of characterization data is linked to computational prediction and modeling or simulation of catalyst behavior, reactor performance, and kinetics. Validation of developed models is often based on experimental characterization data, while typically metadata is not considered, or included to a very limited extent. We expect that in future models have to be applied which rather do not simply take single parameters as input information from characterization, rather a more holistic view on characterization techniques is required. For example, a full pore size distribution together with metadata information about measurement conditions, data analysis pathways and assumption in those should be considered. This approach might not be directly valuable for single cases or shows directly visible results but are a prerequisite to evaluate these often-unseen influences during future big data analysis.

In summary, there is a clear need to progress towards a future in which catalysis research is guided by data rather than trial and error approaches. This is relevant to all stages of the catalyst life cycle, from synthesis, to activation, to stable and consistent performance for a target process. Characterization holds the key to unlock this door, but efforts are required to develop more accurate and meaningful use of catalyst characterization data. This will ideally include the use of reference materials between different instruments and reactor systems, incorporation of data from multiple sources for a single target property, and a better appreciation of physical accuracy and

not only statistical precision in catalyst characterization. The community must be ready to meet these challenges through concerted collaborative efforts.

Conclusions

The present work shows the detailed characterization of an industrial Ni/Al₂O₃ catalyst (SPP2080-IMRC), used within the framework of the collaborative research program SPP2080. The sample is applied as a single batch reference catalyst for CO₂ methanation to exclude or minimize the influence of synthesis history on the material properties. This approach permits a detailed investigation of characterization as a central pillar of catalysis research. The aim is to identify the near future challenges of rational catalyst design and targeted process optimization in heterogeneous catalysis research. The concept of using a singular defined reference catalyst across many different research groups, different instrumental setups, and investigation by a variety of characterization techniques, is rare in academic catalysis research. Furthermore, the present work is the basis for future more detailed studies of the SPP2080-IMRC under *in situ* and *operando* conditions, including dynamic studies. The characterization data in the present work is mainly focused on (i) pore structure, (ii) Ni particle size distribution and (iii) catalytic performance testing. These were identified as parameters of high importance which likewise can be investigated through a variety of methods. The porosity and Ni particle size distribution analysis clearly revealed limitations of the state-of-the-art reporting of certain material properties, e.g., pore or particle diameter. It is to be expected that the common reporting and usage of single mean values, with precision in terms of standard deviation, is limited in its application to create "digital twins". As a prominent example, this was clearly shown by immense differences in the porosity characterization between advanced 3D imaging techniques and conventional methods. The future challenge will be to define different ways of reporting relevant information about a material with accessible metadata, as the accuracy of the information is important for a true "digital twin". This challenge can only be solved by the whole catalysis community and is not feasible through the efforts of individual groups acting alone. The present reference catalyst is an ideal candidate to find solutions for many questions in the frame of digitization in catalysis and should be a stimulation for others to find and apply reference materials for certain reactions. In future, the present knowledge has to be enhanced by further *in situ* and *operando* studies to understand the catalyst structure under reaction conditions. Finally, this showcase may in future lead to the creation of a "digital twin" of the catalyst which can then be further taken as input for rational catalyst design or process optimization, becoming a suitable guiding example for the catalysis community.

Experimental Section

H₂ Temperature-Programmed Reduction (TPR)

H₂-TPR analysis was performed on a BELCAT II catalyst analyzer (MicrotracBEL Corp.) equipped with a thermal conductivity detector (TCD) and a H₂O trap. For a typical experiment, 50 mg catalyst was placed inside the quartz glass reactor. The sample was activated at 573 K for 15 min in an O₂-Ar mixture ($F_{O_2}/F_{Ar}=1/4$) of a total flow rate of 30 cm³ min⁻¹. Then, the flow was switched to pure Ar with a total flow rate of 20 cm³ min⁻¹, and the instrument was allowed to equilibrate for 20 min. Finally, using a H₂-Ar mixture ($F_{H_2}/F_{Ar}=1/9$) and a total flow rate of 30 cm³ min⁻¹, the reactor was heated to 1273 K at a heating rate of 10 K min⁻¹ and kept at the final temperature for 20 min.

H₂ Chemisorption

Pulsed H₂ chemisorption experiments were carried out using a Quantachrome Autosorb iQ-AG (Quantachrome, USA) instrument equipped with a thermal conductivity detector (TCD). 50 mg of the catalyst powder were loaded in the U-shaped reactor of the instrument and held in place with quartz wool. Prior to the measurements, all samples were reduced at 723 K for 10 h (20 K heating ramp) in H₂ (5 vol% in N₂) to ensure full reduction of the catalyst. The sample was subsequently cooled down to 323 K and in total 16 pulses of pure H₂ (262 μL per pulse) were injected into a N₂ carrier gas stream (35 mL min⁻¹), monitoring the H₂ consumption with the TCD. Next, the sample was heated to 573 K in N₂ for 2 h in order to remove any adsorbed H atoms from the metallic surface, before cooling the sample down again to 303 K to repeat the titration experiment. In total, three consecutive pulsed chemisorption experiments were performed this way. Based on the measured H₂ uptake (n_{H_2}), the Ni surface area (S_{Ni}) was calculated according to Equation (1) assuming dissociative H₂ adsorption on Ni ($z=2$):

$$S_{Ni} = \frac{n_{H_2} N_A z}{m_{cat} \sigma_{Ni}} \quad (1)$$

Here, N_A represents Avogadro's constant, m_{cat} the mass of the catalyst sample, and σ_{Ni} the assumed number of surface atoms per unit area (15.4 Ni atoms nm⁻²).^[48] Further, the Ni dispersion (D_{Ni}) was determined by Equation (2) taking the molecular weight of Ni ($M_{Ni}=58.71$ g mol⁻¹) and the Ni weight fraction in the catalyst ($w_{Ni}=0.09$) into account.

$$D_{Ni} = \frac{n_{H_2} z M_{Ni}}{w_{Ni}} \quad (2)$$

CO₂ Chemisorption and Temperature-Programmed Desorption (CO₂-TPD)

A pulsed CO₂ chemisorption immediately followed by a temperature-programmed desorption experiment was performed on the same instrument as the H₂ chemisorption measurements. Here, 100 mg of the catalyst powder was used, loaded in the U-shaped reactor and reduced in an analogous manner to the H₂ chemisorption experiments. After reductive pre-treatment, the sample was cooled down to 303 K and 7 pulses of pure CO₂ (272 μL per pulse) were injected into a He gas stream (35 mL min⁻¹). The reactor was flushed for 10 min to remove any residual CO₂, before

ramping up the temperature (20 K min⁻¹) to 773 K in He while detecting desorbing species with the TCD.

Diffuse Reflectance Infrared Fourier Transformed Spectroscopy (DRIFTS)

DRIFTS measurements were performed to complement the CO₂ chemisorption experiments using a Varian-670 FT-IR spectrometer equipped with a liquid nitrogen cooled MCT detector and an IR cell in praying mantis geometry (VC-DRM-5, Harrick). All spectra were recorded with a resolution of 4 cm⁻¹ in absorbance mode and the average of 128 scans (acquisition time: 78 sec) is shown here. As the DRIFTS cell could not reach the required temperature for the reduction of the catalyst, the pellets were reduced *ex situ* at 723 K for 10 h in flowing H₂, removed at room temperature and subsequently quickly transferred to the DRIFTS cell under exclusion of air. Only when mounting the sample in the IR cell, exposure to air could not be avoided for a short time. Afterwards, the sample compartment was flushed with He to remove any air and the samples were subjected to an additional *in situ* activation step at 673 K in 20 vol% H₂/He (total flow rate: 100 mL min⁻¹) for 60 min (heating time: 30 min). After activation, the samples were cooled down to 303 K in He and the background was acquired. To determine the CO₂ adsorption configuration the sample was exposed to 2 vol% CO₂ in He at a total flowrate of 100 mL min⁻¹ for 120 min during which several spectra were collected. The acquired spectra were processed with the LabSpec5 (Horiba) software. A careful background correction was performed before deconvoluting the spectra using the Gauss-Lorentzian model.

Hg Porosimetry

Hg porosimetry analysis was conducted on a Pascal 140 (ThermoScientific, Waltham, MA, USA) for data points from pressures up to 250 kPa and a Pascal 440 (ThermoScientific, Waltham, MA, USA) for data points from pressures between 250 kPa to 400 MPa. The contact angle used was 140° with a surface tension of 0.48 N m⁻¹. The pore width was calculated by the Washburn equation from the intrusion curve.^[49] The meso- and macropore width with the maximum differential pore volume are referred to as modal mesopore width ($w_{p,meso}$) and modal macropore width ($w_{p,macro}$), respectively. An experimental error of 5% is expected for specific pore volumes and pore widths. Prior to analysis, some part of the material was crushed in a Retsch PM 100 planetary ball mill at 450 rpm for 5 min with ZrO₂ balls. A sieve fraction of 100–300 μm diameter was then used for the "powder" sample analysis additionally to pellets.

Inductively Coupled Plasma Optical Emission Spectrometry (ICP-OES)

ICP-OES was conducted using a Optima 8000 instrument (Perkin Elmer Waltham, MA, USA) equipped with a Scott/crossflow sample injection system. Samples were dissolved in a mixture of hydrofluoric (47–51 wt.%, Normatom, VWR, Radnor, PA, USA), nitric (67–90 wt.%, Normatom, VWR, Radnor, PA, USA), and hydrochloric acid (34–37 wt.%, Normatom, VWR, Radnor, PA, USA) in an Multiwave 3000 (Anton Paar, Graz, Austria) microwave prior to analysis.

N₂ Sorption

N₂ sorption experiments were conducted on a BELSORP-miniX equipment. Samples were degassed at 523 K for at least 6 h. The adsorption and desorption isotherms were recorded at 77 K and

analyzed using the BELSORP BELMaster™ software (total pore volume determined at $p/p_0 \geq 0.99$). Specific surface area and pore width distribution were determined by the BET method^[50] ($p/p_0 = 0.05\text{--}0.30$, adsorption branch) and BJH method^[51] (desorption branch), respectively. An experimental error of 5% is expected for specific surface area, specific pore volume, and pore width. Pellet and powder (see Hg porosimetry) samples were used for analysis.

He Pycnometry

He pycnometry was performed on a Pycnomatic ACT EVO instrument (Porotec, Germany) at room temperature. For analysis, at least 10 pulses of He with a gas pressure of 2 bar were used. The final skeletal density was calculated by taking the average value of at least four consecutive measurements with an experimental error of 0.001 g cm^{-3} . The total porosity (ϵ_{tot}) of the sample was calculated from Equation (3) using the skeletal density (ρ), determined via He pycnometry, and the total specific pore volume ($V_{\text{p,tot}}$), determined from Hg porosimetry. The meso- and macroporosity were calculated likewise, using the specific mesopore and specific macropore volume in the numerator, respectively.

$$\epsilon_{\text{tot}} = \frac{V_{\text{p,tot}}}{V_{\text{p,tot}} + \frac{1}{\rho}} \cdot 100\% \quad (3)$$

Scanning Electron Microscopy (SEM) Imaging

SEM imaging was performed with a Leo 1530 instrument from Zeiss company operated at 5 kV acceleration voltage and equipped with an Everhart-Thornley and inlens detector for secondary electron detection. The spheres were cut and fixed on SEM sample holder with conductive carbon glue. For conductivity the samples were sputtered with gold using a Balzers MED 010 sputter coater.

Powder X-ray Diffraction (PXRD) and Pair Distribution Function (PDF) Analysis

Powder X-ray diffraction (PXRD) data was acquired at PETRA III beamline P21.1 at DESY in Hamburg (Germany). The X-ray energy was 102 keV (wavelength of 0.1215 \AA) and the powder diffraction patterns were collected using a Perkin Elmer XRD1621. The powder was measured in quartz capillaries (WJM-Glas, Berlin, Germany) of 1 mm diameter with 1 s exposure time per pattern. The sample was activated *in situ* using a hot-air blower available at the beamline, while gases were dosed using a custom-made gas-dosing system of mass flow controllers (Bronkhorst) and on-line gas analysis was done using an OMNI-Star GSD 320 mass spectrometer (Pfeiffer Vacuum). The temperature of the hot-air blower was calibrated before the experiment, using a Type-K thermocouple inside an empty capillary. For activation the catalyst was heated from room temperature to 773 K with 10 K min^{-1} with a total flow of 10 mL 25% $\text{H}_2/75\% \text{He}$, and hold for 1 h before cooling to 673 K to analyze the activated catalyst presented in this study. The collected 2D powder patterns were radially integrated using xpdtools,^[52] and the pair distribution function (PDF) was calculated with PDFgetX3.^[53] The PDF modelling was done using DiffPy-cmi.^[54]

Scanning Transmission Electron Microscopy (STEM) and Electron Tomography (ET)

STEM and ET experiments were performed on a Thermo Fisher Scientific Themis 300 equipped with probe corrector and operated at 300 kV in STEM mode with a convergence angle of 21.5 mrad, a

nominal beam diameter of 0.1 nm and a beam current of 154 pA. STEM and ET analysis were performed on a spent catalyst sample after activation (2 h, 773 K, 25% $\text{H}_2/75\% \text{He}$) and catalytic testing at three different temperatures (523, 623, 673 K) with increasing temperature steps (each 1 h, 20% $\text{H}_2/5\% \text{CO}_2/75\% \text{He}$). The catalyst was tested in a continuous flow type laboratory reactor as described in Ref. [26].

Eight different high-angle annular dark field (HAADF)-STEM images were used for particle size analysis with magnifications in the range of 2.75 to 5.50 Mx. Particle size analysis was performed using ImageJ.^[55] A Gaussian blurred background of the image was subtracted from the original image to allow for threshold-based Ni particle labelling. The contours of identified Ni particles were checked with the original images to manually remove artefacts and incorrectly identified labels. The area of the particles was determined, and the particle size was approximated assuming spherical particles for in total 875 labelled particles.

Samples for ET were ground in an agate mortar and suspended in EtOH to add a droplet of the suspension on a 100×400 mesh carbon-coated Cu-TEM grid (Quantifoil Micro Tools GmbH) with a support film thickness of 10–20 nm. Subsequent to drying under atmospheric conditions for 30 min, 6 nm diameter Au colloidal particles were added. ET measurements were performed with a Fischione 2020 tomography holder (Fischione Instruments). Tilt series of HAADF-STEM images were acquired for two particles with the Xplore3D software 3.1 (FEI Company) over a tilt range of -74 to 76° (-68 to 76° used for reconstruction) for ET1 and -66 to 78° (-60 to 74° used for reconstruction) for ET2 in 2° increments. The tilt series was aligned using IMOD^[56] with 20 Au particles as fiducial markers, their position was manually refined, allowing for refinement of image rotation and magnification. The mean residual alignment errors were 0.20 and 0.18 nm for ET1 and ET2, respectively. After 100 iterations of a simultaneous iterative reconstruction technique (SIRT),^[57] the reconstructions were denoised using the “Median 3D” and “Enhance Local Contrast (ELAHE)” plugins of ImageJ.^[55] After applying 10 iterations of discrete algebraic reconstruction technique (DART)^[58] implemented in the “TomoJ” plugin,^[59] the final reconstructions were obtained. The reconstructed isotropic voxel sizes are 0.29 nm (ET1) 0.58 nm (ET2).

Holographic X-ray Computed Tomography (HXCT)

From the same spent catalyst sample as for STEM and ET studies a suitable particle was mounted on an Al tomography pin using a Strata 400 S FIB/SEM (FEI Company). The particle was attached to a micromanipulator by Pt deposition, then transferred and Pt-glued on the Al-pin. The sample on the pin is shown in Figure S2.

The nano-tomographic reconstruction was obtained at the ID16A-NI beamline of the European Synchrotron Radiation Facility (ESRF). The experiment was performed at high energy (17.1 keV) ensuring the transmission of the X-ray across the sample and thus allowing the reconstruction of a large field of view. Two multilayer coated Kirkpatrick-Baez (KB) mirrors are used to focus the X-ray beam down to $\approx 23(\text{h}) \times 37(\text{v})$ nanometers.^[60] This unique nanometric focus size is coupled with very high photon flux (up to 10^{13} photons s^{-1}), high monochromaticity ($\Delta E/E \approx 1\%$) and high spatial coherence thanks to the large propagation distance between the source and the experimental hutch.

The 3D reconstruction was obtained using holographic X-ray computed tomography (HXCT).^[61] Holography is a full-field imaging technique based on the free-space propagation of the X-rays. The projections are obtained with the sample out-of-focus and the radiographs consist in the magnified near-field in-line holograms of

the sample (Fresnel diffraction) containing the information of the phase shift induced by the materials on the X-ray beam. Moreover, taking advantage of the geometric magnification effect of the divergent cone beam, it is possible to select the voxel size in the final reconstruction by changing the relative distance between the sample and the X-ray focal plane. For the tomography reconstruction, 1800 radiographies are acquired over 180° with an exposure time of 0.25 s at four different sample-to-focus positions along the optical axis. This longitudinal diversity allows to enhance the final resolution of the volume thanks to the increase of information.^[62] Moreover, for each angle, random in-plane motions of the samples are added to avoid ring-shaped artifacts in the final 3D volume.^[63]

Once the projections have been acquired, flat-field correction is applied to all the images and the radiographies of the 2nd, 3rd, and 4th distances are resized via interpolation to match the pixel size of the 1st distance, which determines the voxel size in the final reconstruction (25 nm). Afterwards, the resized projections at the four distances are carefully aligned to each other^[64] and the 2D phase map for each angle is determined from the four aligned projections by using an iterative phase-retrieval procedure implemented in GNU Octave.^[65,66] The final tomographic reconstruction is obtained by using the filtered back-projection (FBP) algorithm on the aligned phase maps. This last step is performed using the PyHST software package developed at the ESRF.^[67] The final volume is a 3D map in which the value in each voxel is a quantitative representation of the real part of the local refractive index decrement (δ), which is proportional to the electron density.^[68] The spatial resolution in the final 3D volume has been measured by analyzing the edge profile at the interface between two material phases. The measured data have been fitted with a hyperbolic tangent function and a 10–90% criterion was applied to determine the physical resolution in the volume.^[69] The same procedure has been applied on different interfaces to be statistically representative. Using this methodology, a mean value of ≈ 94 nm was found whereas the best value was ≈ 54 nm corresponding to approximately two voxels (see Figure S3).

X-ray Microtomography (μ -XCT)

μ -XCT analysis was performed using a Zeiss Xradia Versa 520 X-ray microscope (Pleasanton, United States). The sample was scanned using a 4X objective lens in binning 2 mode with a tungsten X-ray source. The instrument was operated at 40 kV and 76 μ A, employing a low energy filter to optimize transmission and signal to noise ratio. The chosen setting provided an optical magnification of 3.95 and voxel size of 2.67 μ m. The sample was scanned within the entire range of 0–360° and 2041 images were acquired with an exposure time of 1 s per image. The scanning time highly depends on number of recorded projections and exposure time. This parameter setting led to a scanning time around 2 h.

Reconstructions were done manually with a commercial software package (Zeiss XMReconstructor), which uses an algorithm based on standard filtered back-projection. The procedure for manual reconstruction consists of two main steps: finding the correct value for center of rotation and the beam hardening constant. The center shift value is the amount, in pixels, that the axis of rotation is offset from the detector's center column. Images with incorrect center shift are unfocused and blurry, while images with correct center shift are focused and clear, with clean edge features. Beam hardening effect results in non-uniform intensity signals in reconstructed views where the sample density remains the same. Therefore, in order to reduce this artifact, the proper correction constant should be selected and performed on a focused image.

Image Analysis of ET, HXCT and μ -XCT

Image analysis of the reconstructed ET, HXCT and μ -XCT was performed with Avizo v.9.7.0 (Thermo Fisher Scientific). First the tomograms were masked from the surrounding air by *thresholding*, *lasso* and *interpolation* tools of the segmentation editor to obtain a whole particle label. Afterwards, the particle label was segmented by thresholding into solid and pore labels (for ET thresholding is performed only to assign the labels). *Closing* and *opening* modules were used to remove segmentation artefacts as indicated in brackets from the solid (ET1: *closing* 1 px, *opening* 1 px; ET2: *closing* 1 px, *opening* 1 px; HXCT: *opening* 1 px) and pore labels (ET1: *opening* 3 px; ET2: *opening* 2 px; HXCT: *opening* 1 px). The pore label was further separated into individual labelled pores using the *separate objects* module (ET1: *skeleton-aggressive*, *marker extent* = 1 px; ET2: *skeleton-aggressive*, *marker extent* = 1 px; HXCT: *chamfer-conservative*, *marker extent* = 1 px). The solid, pores and separated pore labels were quantitatively analyzed using the *label analysis* module, solid (Volume3D, Area3D, BaryCenterX, BaryCenterY, BaryCenterZ), total pores (Volume3D, Area3D), separated pores (Area3D, d_{eq} , Volume3D, Sphericity, Length3D, Width3D, AspectRatio, BaryCenterX, BaryCenterY, BaryCenterZ). For the two ET the separated pore labels were used to derive a pore network model by the *generate pore network model* module, which results in labelled spherical pores and cylindrical throats connecting the pores. For each spherical pore an equivalent spherical diameter (d_{eq} , Eq. (5)) analysis was performed, while for each throat the cylindrical throat diameter (d_{throat}) was derived.

Statistical analysis and visualization of the retrieved quantitative image analysis results was performed with python-scripts using NumPy,^[70] SciPy^[71] and matplotlib^[72] packages. Statistical analysis mainly consisted of the porosity / pore volume and throat volume weighted distribution analysis of d_{eq} and d_{throat} .

The porosity for each tomogram (ϵ_{tomo}) was calculated according to the following Equation (4):

$$\epsilon_{\text{tomo}} = \frac{V_{\text{pores}}}{V_{\text{pores}} + V_{\text{solid}}} \cdot 100\% \quad (4)$$

With V_{pores} as the volume of the pore label and V_{solid} the volume of the (nanoporous) solid label in the tomogram. For the separated pore labels the equivalent spherical pore diameter (d_{eq}) was calculated according to the following relation [Eq. (5)]:

$$d_{\text{eq}} = \sqrt[3]{\frac{6 V_{\text{pore}}}{\pi}} \quad (5)$$

With V_{pore} as the volume of an individual pore. The macroporosity (ϵ_{M}) based on the tomography studies is defined as the ϵ_{tomo} obtained from HXCT. The mesoporosity (ϵ_{m}) is calculated using the average ϵ_{tomo} of the two ET and considering this average porosity as the porosity value of the nanoporous solid label of the HXCT.

Catalytic Activity Measurements

To perform catalytic activity measurements, three catalyst particle spheres with a total weight of 30.3 mg are placed into a quartz glass tube with an inner diameter of 8 mm, an outer diameter of 10 mm, and a length of 40 cm. Each catalyst particle sphere is separated by a quartz glass bead with a diameter of about 2.5 mm, as shown in FigureS 1a, ESI. The spheres are fixed with quartz glass wool from both sides. Additionally, 0.5 g silicon carbide is placed in front of the catalyst spheres, to ensure isothermal and uniformly distributed gas flow. The silicon carbide is also kept in place by

quartz glass wool. Type K thermocouples are placed before and behind the packing. The latter is considered as reaction temperature. The setup is also used with the same mass of powder (415–500 μm sieve fraction) of crushed catalyst spheres, which was diluted with a 1:9 ratio in silicon carbide powder (Figure S1b).

After the glass tube is placed into a furnace and sealed, gases (CO_2 3.0, H_2 5.0, He 5.0, Westfalen AG) are supplied via mass flow controllers (El-Flow® Select, Bronkhorst Deutschland Nord GmbH). The product gas is cooled down to 276 K to condensate water and a constant flow of 15 Nml min^{-1} nitrogen (N_2 5.0, Westfalen AG) is added as internal standard. Potentially remaining water is separated with a membrane before the product gases, in particular the flow rates of CO_2 , CO, CH_4 , are determined by gas chromatography (490 Micro GC System, Agilent Technologies, Inc.).

Before the catalytic activity measurements are conducted, the catalyst is dried at a furnace temperature of 393 K with 120 Nml min^{-1} of a 1:1 mixture of H_2 and He. Afterwards, the furnace temperature is increased to 673 K and the catalyst is reduced for eight hours under the same gas composition. Subsequently, the catalyst is aged at reaction conditions ($F_{\text{CO}_2} = 20 \text{ Nml min}^{-1}$, $F_{\text{H}_2} = 80 \text{ Nml min}^{-1}$, $F_{\text{He}} = 100 \text{ Nml min}^{-1}$, $p = 1.2 \text{ bar(a)}$) at 773 K for eight hours. Five product gas samples are taken at each furnace temperature, following a step change profile from 773 to 523 K in steps of 25 K. The temperature difference before and behind the packing is below 7 K and the furnace temperature is up to 15 K higher than the reaction temperature. The carbon balance is closed to more than 99% in all cases.

Catalytic Tests in a Parallel Testing Unit

Catalytic tests were carried out in an in-house developed set-up containing 50 continuous-flow fixed-bed stainless-steel tubular (inner diameter 4 mm, length of 235 mm) reactors. The total feed flow was equally distributed among the reactors. In a typical test, the catalyst (425–450 μm fraction) diluted by SiC with a mass ratio of 1:9 was loaded within the isothermal zone of the reactor. To achieve different degrees of CO_2 conversion, different catalyst amounts (0.025, 0.05, 0.075, 0.1, 0.125 and 0.15 g) were used. Before starting the methanation reaction, each catalyst sample was reduced *in situ* at 673 K and 1 bar in a flow of $\text{H}_2/\text{N}_2 = 1/1$ (12 mL min^{-1} per reactor) for 4 h. Then, the reactors were cooled to 523 K (1 K min^{-1}) in N_2 followed by feeding a $\text{H}_2/\text{CO}_2/\text{N}_2 = 0.8/0.2/9$ mixture with a flow rate of 12 mL min^{-1} per reactor and increasing the pressure to 10 bar. Outlet gases after each reactor were analyzed five times with 7 h intervals between each measurement. In total, the catalyst was tested for 28 h on stream at this temperature. Hereafter, the temperature was initially reduced to 498, 473 K and then increased to 548 and 573 K, and finally decreased back to 523 K. The feed flow was not interrupted upon temperature changes. The tests at each temperature were carried out as at 523 K.

The feed components and the reaction products were analyzed by an on-line Agilent 7890A gas chromatograph equipped with a flame ionization detector (FID) and a thermal conductivity detector (TCD). HP Plot/Q (for CO_2) and MolSieve 5A (for H_2 , O_2 , N_2 , CH_4 and CO) columns are connected to TCD, while AL/S and FFAP columns are connected to FID for separating C_1 – C_8 and C_9 – C_{18} hydrocarbons, respectively. To avoid condensation of higher hydrocarbons, stainless steel lines between the reactor outlet and the GC inlet were heated to around 453 K. The conversion of CO_2 ($X(\text{CO}_2)$) and selectivity to each gas-phase product ($S(i)$) were calculated by Equations (6) and (7):

$$X(\text{CO}_2) = 1 - \frac{\dot{n}_{\text{CO}_2}^{\text{out}}}{\dot{n}_{\text{CO}_2}^{\text{in}}} \quad (6)$$

$$S(i) = \frac{a_i \dot{n}_i^{\text{out}}}{\sum_{i=1}^n a_i \dot{n}_i^{\text{out}}} \quad (7)$$

where $\dot{n}_{\text{CO}_2}^{\text{in}}$ and $\dot{n}_{\text{CO}_2}^{\text{out}}$ stand for the molar fraction of CO_2 in the inlet and outlet gas, respectively. $S(i)$ is the selectivity to product i , a_i is the carbon number in each product. \dot{n}_i with superscripts 'in' and 'out' is the fraction of product i at the reactor inlet and outlet, respectively. Reaction-induced changes in the number of moles were taken into account by using N_2 as an internal standard.

Author Contributions

SeW and TS contributed sample preparation for HXCT, ET reconstruction, image analysis of ET, HXCT, μ -XCT and STEM data, PDF data collection, discussion of results, managing the manuscript. RZ, JB and KS contributed the reference catalyst, catalytic activity measurements and analysis, analysis of TPR data, discussion of results. KA, DP and RG contributed the conventional porosity analysis, SEM images, elemental analysis, TPR data, discussion of results. NP and MZ contributed PDF data analysis, discussion of results. JI and MarB contributed H_2 chemisorption, CO_2 TPD and DRIFTS analysis, discussion of results. SvW and MatB contributed XAS data collection and analysis, discussion of results and text. QY and EVK contributed parallel catalytic testing, data analysis and discussion. RP contributed μ -XCT data collection and reconstruction. FM and PC contributed HXCT data collection and reconstruction, discussion of results. XH and CK contributed STEM and ET data collection, discussion of results. All authors contributed reviewing and writing of the manuscript.

Acknowledgements

Gefördert durch die Deutsche Forschungsgemeinschaft (DFG) – 406914011, KO 2261/10-1, ZO 369/2-1, BA 1710/31-1 funded by the Deutsche Forschungsgemeinschaft (DFG, German Research Foundation) – 406914011, KO 2261/10-1, ZO 369/2-1, BA 1710/31-1. We acknowledge discussion of the results with Jan-Dierk Grunwaldt in the frame of the SPP2080 project by the DFG. Generous supply of SPP2080-IMRC by our industrial partner is gratefully acknowledged. We acknowledge DESY (Hamburg, Germany), a member of the Helmholtz Association HGF, for the provision of experimental facilities. Parts of this research were carried out at PETRA III beamline P21.1. Beamtime was allocated for proposal I-20200385. Thanks to Philipp Glaevecke, Soham Banerjee, Olof Gutowski, Linda Klag and Srashtasrita Das for support during beamtime. The holographic X-ray computed tomography experiments were performed on beamline ID16A at the European Synchrotron Radiation Facility (ESRF), Grenoble, France in the frame of experiment CH-5805. This work was partly carried out with the support of the Karlsruhe Nano Micro Facility (KNMF), a Helmholtz Research Infrastructure at Karlsruhe Institute

of Technology (KIT), which provided access to FIB and TEM instruments via proposal 2020-023-028494. Thanks to Mariam Schulte for performing catalytic experiments of the TEM sample. Thanks to Sabine Schlachbach for support during FIB sample preparation. Ronny Zimmermann is also affiliated with the International Max Planck Research School (IMPRS) for Advanced Methods in Process and Systems Engineering, Magdeburg, Germany. Xiaohui Huang acknowledges the China Scholarship Council for providing a PhD scholarship. Open Access funding enabled and organized by Projekt DEAL.

Conflict of Interest

The authors declare no conflict of interest.

Data Availability Statement

X-ray holotomography and electron tomography data that support the findings of this study are openly available in KIOpen at (10.5445/IR/1000141008 and 10.5445/IR/1000140987), reference numbers (1000141008 and 1000140987). All other data that support the findings of this study are available in the supplementary material of this article, or on request from the authors.

Keywords: characterization · digitization · methanation · nickel · reference catalyst

- [1] R. Schlögl, *ChemCatChem* **2017**, *9*, 533–541.
- [2] C. Wulf, M. Beller, T. Boenisch, O. Deutschmann, S. Hanf, N. Kockmann, R. Kraehnert, M. Oezaslan, S. Palkovits, S. Schimmler, S. A. Schunk, K. Wagemann, D. Linke, *ChemCatChem* **2021**, *13*, 3223–3236.
- [3] “NFDI4Cat - NFDI für Wissenschaften mit Bezug zur Katalyse,” can be found under <https://gepris.dfg.de/gepris/projekt/441926934?context=projekt&task=showDetail&id=441926934&>, **2021**.
- [4] “European Commission: Funding & tender opportunities, Online Manual,” can be found under <https://webgate.ec.europa.eu/funding-tenders-opportunities/display/OM/Online+Manual>, **2021**.
- [5] K. F. Kalz, R. Kraehnert, M. Dvovashkin, R. Dittmeyer, R. Gläser, U. Krewer, K. Reuter, J. D. Grunwaldt, *ChemCatChem* **2017**, *9*, 17–29.
- [6] “DFG Priority Program SPP 2080 – Catalysts and reactors under dynamic conditions for energy storage and conversion” can be found under <https://www.itcp.kit.edu/spp2080/english/index.php>, **2021**.
- [7] M. Thommes, K. Kaneko, A. V. Neimark, J. P. Olivier, F. Rodriguez-Reinoso, J. Rouquerol, K. S. W. Sing, *Pure Appl. Chem.* **2015**, *87*, 1051–1069.
- [8] C. Schlumberger, M. Thommes, *Adv. Mater. Interfaces* **2021**, *8*, 2002181.
- [9] S. Mitchell, N. L. Michels, K. Kunze, J. Pérez-Ramírez, *Nat. Chem.* **2012**, *4*, 825–831.
- [10] S. Mitchell, N. L. Michels, G. Majano, J. Pérez-Ramírez, *Curr. Opin. Chem. Eng.* **2013**, *2*, 304–311.
- [11] I. L. C. Buurmans, B. M. Weckhuysen, *Nat. Chem.* **2012**, *4*, 873–886.
- [12] F. Meirer, B. M. Weckhuysen, *Nat. Rev. Mater.* **2018**, *3*, 324–340.
- [13] F. Tariq, R. Haswell, P. D. Lee, D. W. McComb, *Acta Mater.* **2011**, *59*, 2109–2120.
- [14] F. Tariq, P. D. Lee, R. Haswell, D. W. McComb, *Chem. Eng. Sci.* **2011**, *66*, 5804–5812.
- [15] S. Weber, K. L. Abel, R. T. Zimmermann, X. Huang, J. Bremer, L. K. Rihko-Struckmann, D. Batey, S. Cipiccia, J. Titus, D. Poppitz, C. Kübel, K. Sundmacher, R. Gläser, T. L. Sheppard, *Catalysts* **2020**, *10*, 1–22.
- [16] J. C. da Silva, K. Mader, M. Holler, D. Haberthür, A. Diaz, M. Guizar-Sicarios, W. C. Cheng, Y. Shu, J. Raabe, A. Menzel, J. A. van Bokhoven, *ChemCatChem* **2015**, *7*, 413–416.
- [17] Y. Fam, T. L. Sheppard, A. Diaz, T. Scherer, M. Holler, W. Wang, D. Wang, P. Brenner, A. Wittstock, J. D. Grunwaldt, *ChemCatChem* **2018**, *10*, 2858–2867.
- [18] J. Becher, T. L. Sheppard, Y. Fam, S. Baier, W. Wang, D. Wang, S. Kulkarni, T. F. Keller, M. Lyubomirskiy, D. Brueckner, M. Kahnt, A. Schropp, C. G. Schroer, J. D. Grunwaldt, *J. Phys. Chem. C* **2019**, *123*, 25197–25208.
- [19] T. Li, J. Ihli, Z. Ma, F. Krumeich, J. A. van Bokhoven, *J. Phys. Chem. C* **2019**, *123*, 8793–8801.
- [20] S. H. Lee, W. S. Chang, S. M. Han, D. H. Kim, J. K. Kim, *J. Membr. Sci.* **2017**, *535*, 28–34.
- [21] E. Gregorová, T. Uhlířová, W. Pabst, P. Diblíková, I. Sedlářová, *Ceram. Int.* **2018**, *44*, 12315–12328.
- [22] Q. Xiong, T. G. Baychev, A. P. Jivkov, *J. Contam. Hydrol.* **2016**, *192*, 101–117.
- [23] B. Priffling, M. Neumann, D. Hlushkou, C. Kübel, U. Tallarek, V. Schmidt, *Comput. Mater. Sci.* **2021**, *187*, 1–21.
- [24] Y. Liu, F. Meirer, C. M. Krest, S. Webb, B. M. Weckhuysen, *Nat. Commun.* **2016**, *7*, DOI 10.1038/ncomms12634.
- [25] L. Smrčok, V. Langer, J. Křestán, *Acta Crystallogr. Sect. C* **2006**, *62*, i83–i84.
- [26] B. Mutz, M. Belimov, W. Wang, P. Sprenger, M.-A. Serrer, D. Wang, P. Pfeifer, W. Kleist, J.-D. Grunwaldt, *ACS Catal.* **2017**, *7*, 6802–6814.
- [27] M. A. Newton, S. Checchia, A. J. Knorpp, D. Stoian, W. Van Beek, H. Emerich, A. Longo, J. A. Van Bokhoven, *Catal. Sci. Technol.* **2019**, *9*, 3081–3089.
- [28] R. W. Cairns, E. Ott, *J. Am. Chem. Soc.* **1933**, *376*, 527–533.
- [29] S. Schuster, E. Klemm, M. Bauer, *Chem. Eur. J.* **2012**, *18*, 15831–15837.
- [30] M. A. Gotthardt, R. Schoch, S. Wolf, M. Bauer, W. Kleist, *Dalton Trans.* **2015**, *44*, 2052–2056.
- [31] N. Prinz, L. Schwensow, S. Wendholt, A. Jentys, M. Bauer, W. Kleist, M. Zobel, *Nanoscale* **2020**, *12*, 15800–15813.
- [32] A. Anspoks, A. Kalinko, R. Kalendarev, A. Kuzmin, *Phys. Rev. B: Condens. Matter Mater. Phys.* **2012**, *86*, 174114.
- [33] T. Costanzo, F. Benzi, P. Ghigna, S. Pin, G. Spinolo, F. D’Acapito, *J. Synchrotron Radiat.* **2014**, *21*, 395–400.
- [34] A. Anspoks, A. Kuzmin, A. Kalinko, J. Timoshenko, *Solid State Commun.* **2010**, *150*, 2270–2274.
- [35] T. Shido, M. Lok, R. Prins, *Top. Catal.* **1999**, *8*, 223–236.
- [36] C. Li, Y. W. Chen, *Thermochim. Acta* **1995**, *256*, 457–465.
- [37] X. Xu, L. Li, F. Yu, H. Peng, X. Fang, X. Wang, *J. Mol. Catal.* **2017**, *441*, 81–91.
- [38] B. Kreitz, A. M. Arias, J. Martin, A. P. Weber, T. Turek, *Catalysts* **2020**, *10*, 1410.
- [39] D. Beierlein, D. Häussermann, M. Pfeifer, T. Schwarz, K. Stöwe, Y. Traa, E. Klemm, *Appl. Catal. B* **2019**, *247*, 200–219.
- [40] J. Ilsemann, M. M. Murshed, T. M. Gesing, J. Kopyscinski, M. Bäumer, *Catal. Sci. Technol.* **2021**, *11*, 4098–4114.
- [41] Q. Pan, J. Peng, T. Sun, S. Wang, S. Wang, *Catal. Commun.* **2014**, *45*, 74–78.
- [42] M. A. Vasiliades, C. M. Kalamaras, N. S. Govender, A. Govender, A. M. Efstathiou, *J. Catal.* **2019**, *379*, 60–77.
- [43] X. Wang, H. Shi, J. H. Kwak, J. Szanyi, *ACS Catal.* **2015**, *5*, 6337–6349.
- [44] C. Morterra, G. Magnacca, *Catal. Today* **1996**, *27*, 497–532.
- [45] J. Szanyi, J. H. Kwak, *Phys. Chem. Chem. Phys.* **2014**, *16*, 15117–15125.
- [46] T. Burger, P. Donaubaauer, O. Hinrichsen, *Appl. Catal. B* **2021**, *282*, 119408.
- [47] J. A. Hernandez Lalinde, P. Roongruangsree, J. Ilsemann, M. Bäumer, J. Kopyscinski, *Chem. Eng. J.* **2020**, *390*, 124629.
- [48] S. Tada, M. Yokoyama, R. Kikuchi, T. Haneda, H. Kameyama, *J. Phys. Chem. C* **2013**, *117*, 14652–14658.
- [49] E. W. Washburn, *Phys. Rev.* **1921**, *17*, 273–283.
- [50] S. Brunauer, P. H. Emmett, E. Teller, *J. Am. Chem. Soc.* **1938**, *60*, 309–319.
- [51] E. P. Barrett, L. G. Joyner, P. P. Halenda, *J. Am. Chem. Soc.* **1951**, *73*, 373–380.
- [52] C. J. Wright, X. D. Zhou, *J. Synchrotron Radiat.* **2017**, *24*, 506–508.
- [53] P. Juhás, T. Davis, C. L. Farrow, S. J. L. Billinge, *J. Appl. Crystallogr.* **2013**, *46*, 560–566.
- [54] P. Juhás, C. L. Farrow, X. Yang, K. R. Knox, S. J. L. Billinge, *Acta Crystallogr. Sect. A* **2015**, *71*, 562–568.
- [55] J. Schindelin, I. Arganda-Carreras, E. Frise, V. Kaynig, M. Longair, T. Pietzsch, S. Preibisch, C. Rueden, S. Saalfeld, B. Schmid, J.-Y. Tinevez,

- D. J. White, V. Hartenstein, K. Eliceiri, P. Tomancak, A. Cardona, *Nat. Methods* **2012**, *9*, 676–682.
- [56] J. R. Kremer, D. N. Mastrorade, J. R. McIntosh, *J. Struct. Biol.* **1996**, *116*, 71–76.
- [57] P. Gilbert, *J. Theor. Biol.* **1972**, *36*, 105–117.
- [58] K. J. Batenburg, S. Bals, J. Sijbers, C. Kübel, P. A. Midgley, J. C. Hernandez, U. Kaiser, E. R. Encina, E. A. Coronado, G. Van Tendeloo, *Ultramicroscopy* **2009**, *109*, 730–740.
- [59] C. Messaoudil, T. Boudier, C. O. S. Sorzano, S. Marco, *BMC Bioinf.* **2007**, *8*, 1–9.
- [60] C. Morawe, R. Barrett, P. Cloetens, B. Lantelme, J.-C. Peffen, A. Vivo, *Proc. SPIE* **2015**, *9588*, 958803.
- [61] P. Cloetens, W. Ludwig, J. Baruchel, D. Van Dyck, J. Van Landuyt, J. P. Guigay, M. Schlenker, *Appl. Phys. Lett.* **1999**, *75*, 2912–2914.
- [62] S. Zabler, P. Cloetens, J. P. Guigay, J. Baruchel, M. Schlenker, *Rev. Sci. Instrum.* **2005**, *76*, 073705.
- [63] M. Hubert, A. Pacureau, C. Guilloud, Y. Yang, J. C. Da Silva, J. Laurencin, F. Lefebvre-Joud, P. Cloetens, *Appl. Phys. Lett.* **2018**, *112*, 203704.
- [64] L. Weber, A. Hänsch, U. Wolfram, A. Pacureau, P. Cloetens, F. Peyrin, S. Rit, M. Langer, *J. Microsc.* **2018**, *269*, 36–47.
- [65] P. Cloetens, W. Ludwig, E. Boller, L. Helfen, L. Salvo, R. Mache, M. Schlenker, *Proc. SPIE* **2002**, *4503*, 82–91.
- [66] B. Yu, L. Weber, A. Pacureau, M. Langer, C. Olivier, P. Cloetens, F. Peyrin, *Opt. Express* **2018**, *26*, 11110–11124.
- [67] A. Mirone, E. Brun, E. Gouillart, P. Tafforeau, J. Kieffer, *Nucl. Instrum. Methods Phys. Res. Sect. B* **2014**, *324*, 41–48.
- [68] A. Diaz, P. Trtik, M. Guizar-Sicairos, A. Menzel, P. Thibault, O. Bunk, *Phys. Rev. B* **2012**, *85*, 1–4.
- [69] M. Holler, A. Diaz, M. Guizar-Sicairos, P. Karvinen, E. Färm, E. Härkönen, M. Ritala, A. Menzel, J. Raabe, O. Bunk, *Sci. Rep.* **2014**, *4*, 1–5.
- [70] C. R. Harris, K. J. Millman, S. J. van der Walt, R. Gommers, P. Virtanen, D. Cournapeau, E. Wieser, J. Taylor, S. Berg, N. J. Smith, R. Kern, M. Picus, S. Hoyer, M. H. van Kerkwijk, M. Brett, A. Haldane, J. F. del Río, M. Wiebe, P. Peterson, P. Gérard-Marchant, K. Sheppard, T. Reddy, W. Weckesser, H. Abbasi, C. Gohlke, T. E. Oliphant, *Nature* **2020**, *585*, 357–362.
- [71] P. Virtanen, R. Gommers, T. E. Oliphant, M. Haberland, T. Reddy, D. Cournapeau, E. Burovski, P. Peterson, W. Weckesser, J. Bright, S. J. van der Walt, M. Brett, J. Wilson, K. J. Millman, N. Mayorov, A. R. J. Nelson, E. Jones, R. Kern, E. Larson, C. J. Carey, Í. Polat, Y. Feng, E. W. Moore, J. VanderPlas, D. Laxalde, J. Perktold, R. Cimrman, I. Henriksen, E. A. Quintero, C. R. Harris, A. M. Archibald, A. H. Ribeiro, F. Pedregosa, P. van Mulbregt, A. Vijaykumar, A. Pietro Bardelli, A. Rothberg, A. Hilboll, A. Kloeckner, A. Scopatz, A. Lee, A. Rokem, C. N. Woods, C. Fulton, C. Masson, C. Häggström, C. Fitzgerald, D. A. Nicholson, D. R. Hagen, D. V. Pasechnik, E. Olivetti, E. Martin, E. Wieser, F. Silva, F. Lenders, F. Wilhelm, G. Young, G. A. Price, G. L. Ingold, G. E. Allen, G. R. Lee, H. Audren, I. Probst, J. P. Dietrich, J. Silterra, J. T. Webber, J. Slavič, J. Nothman, J. Buchner, J. Kulick, J. L. Schönberger, J. V. de Miranda Cardoso, J. Reimer, J. Harrington, J. L. C. Rodríguez, J. Nunez-Iglesias, J. Kuczynski, K. Tritz, M. Thoma, M. Newville, M. Kümmerer, M. Bolingbroke, M. Tartre, M. Pak, N. J. Smith, N. Nowaczyk, N. Shebanov, O. Pavlyk, P. A. Brodtkorb, P. Lee, R. T. McGibbon, R. Feldbauer, S. Lewis, S. Tygier, S. Sievert, S. Vigna, S. Peterson, S. More, T. Pudlik, T. Oshima, T. J. Pingel, T. P. Robitaille, T. Spura, T. R. Jones, T. Cera, T. Leslie, T. Zito, T. Krauss, U. Upadhyay, Y. O. Halchenko, Y. Vázquez-Baeza, *Nat. Methods* **2020**, *17*, 261–272.
- [72] J. D. Hunter, *Comput. Sci. Eng.* **2007**, *9*, 90–95.

Manuscript received: December 9, 2021
Revised manuscript received: February 6, 2022
Accepted manuscript online: February 10, 2022
Version of record online: March 9, 2022